

1 **Monitoring and simulation of salinity changes in response to tide and storm surges in**
2 **a sandy coastal aquifer system**

3 **S. Huizer^{1,2}, M.C. Karaoulis², G. H. P. Oude Essink^{1,2}, and M. F. P. Bierkens^{1,2}**

4 ¹Department of Physical Geography, Utrecht University, Utrecht, Netherlands.

5 ²Department of Subsurface and Groundwater Systems, Deltares, Utrecht, Netherlands.

6 Corresponding author: Sebastian Huizer (s.huizer@uu.nl)

7 **Key Points:**

- 8 • Monitoring effects of tides and storm surges on groundwater salinity with time-lapse
9 electrical resistivity tomography
10 • Observed changes in salinity can be reproduced with a variable-density groundwater model
11 • Incorporation of wave run-up substantially improves the estimation of the extent of land-
12 surface inundations
13

14 **Abstract**

15 Tidal dynamics and especially storm surges can have an extensive impact on coastal fresh
16 groundwater resources. Combined with the prospect of sea-level rise and the reliance of many
17 people on these resources, this demonstrates the need to assess the vulnerability of coastal areas
18 to these threats. In this study we investigated the impact of tides and storm surges on coastal
19 groundwater at a pilot location on the Dutch coast (viz. the Sand Engine). To monitor changes in
20 groundwater salinity under a variety of conditions, we performed automated measurements with
21 electrical resistivity tomography for a period of two months between November 2014 and
22 January 2015. The obtained resistivity images were converted to salinity images, and these
23 images served effectively as observations of the impact of tidal fluctuations, saltwater overwash
24 during storm surges, and the recovery of the freshwater lens after land-surface inundations.

25
26 Most of the observed changes in groundwater head and salinity could be reproduced with a two-
27 dimensional variable-density groundwater flow and salt transport model. This shows that
28 groundwater models can be used to make accurate predictions of the impact of tides and storm
29 surges on fresh groundwater resources, given a thorough understanding of the (local) system.
30 Comparisons of measurements and model simulations also showed that morphological changes
31 and wave run-up can have a strong impact on the extent of land-surface inundations in (low-
32 elevation) dynamic coastal environments, and can therefore substantially affect coastal fresh
33 groundwater resources.

34 **1 Introduction**

35 Most coastal regions in the world rely on groundwater as their main source of fresh water for
36 agricultural, domestic and industrial sectors. However, in many coastal regions the availability of
37 fresh groundwater is threatened by unsustainable levels of groundwater extraction and rising sea-
38 levels [*Ferguson and Gleeson, 2012*]. Combined with the likely continuation of sea-level rise
39 (SLR) and increase in the frequency and intensity of storm surges [*Nicholls, 2010; Wong et al.,*
40 *2014*], this will lead to more seawater intrusion (SWI) in coastal aquifers. One important driver
41 of the increase in SWI will consist of more extensive and frequent land-surface inundations (LSI)
42 [*Ketabchi et al., 2016*]. In particular (low-elevation) coastal groundwater systems with shallow
43 groundwater levels are vulnerable in this respect, because these systems are most susceptible to
44 LSI and SWI [*McGranahan et al., 2007*], and an increase of the groundwater level in response to
45 SLR is restricted [*Michael et al., 2013*]

46
47 These threats and the reliance of many coastal communities on fresh groundwater raises the
48 importance of an optimal management of fresh groundwater in coastal aquifers to control or
49 mitigate salinization [*Khan et al., 2015*]. However, the management of coastal groundwater can
50 be complex, because the extent of LSI and SWI depends on many factors: e.g. groundwater
51 extractions, aquifer hydraulic properties, and coastal hydro- and morphodynamics [*Ferguson and*
52 *Gleeson, 2012; Vallejos et al., 2014*]. Several studies have therefore stressed the importance of
53 intensive monitoring, to acquire more data in different hydrogeological conditions and in real-
54 world coastal aquifers [*Werner et al., 2013; Ketabchi et al., 2016*].

55
56 A promising monitoring technique for LSI and SWI in coastal aquifers is (time-lapse) electrical
57 resistivity tomography (ERT) [*de Franco et al., 2009; Ogilvy et al., 2009; Henderson et al.,*
58 *2010; Morrow et al., 2010; Hermans et al., 2012*]. In ERT, the noninvasive direct current (DC)

59 resistivity method is used to visualize the subsurface resistivity distribution in two- or three-
60 dimensional images [Revil *et al.*, 2012]. One of the main advantages of this method is the ability
61 to conduct automated time-lapse measurements along multi-dimensional arrays, and therefore to
62 provide images of the evolution of the fresh-salt groundwater distributions over time [Ogilvy *et*
63 *al.*, 2009]. Additionally this technique can help to constrain or validate parameters in
64 groundwater models [Comte and Banton, 2007; Nguyen *et al.*, 2009; Beaujean *et al.*, 2014].
65

66 Many studies have addressed the possible effects of climate change and in particular SLR on
67 coastal groundwater resources [Oude Essink *et al.*, 2010; Watson *et al.*, 2010; Chang *et al.*, 2011;
68 Webb and Howard, 2011; Michael *et al.*, 2013]. Most of these studies have neglected LSI [Ataie-
69 Ashtiani *et al.*, 2013], and recent studies have shown that LSI can have a significant impact on
70 SWI in coastal aquifers [Ketabchi *et al.*, 2014; Morgan and Werner, 2014]. LSI is primarily
71 driven by coastal forcing (Figure 1), ranging from tidal fluctuations with a small to negligible
72 impact on the mixing zone, to episodic events such as storm surges that can lead to significant
73 SWI [Ataie-Ashtiani *et al.*, 1999; Wilson *et al.*, 2011]. Many laboratory and modeling studies
74 have examined the impact of coastal hydro- and morphodynamics on aquifers [Robinson *et al.*,
75 2007a; Kuan *et al.*, 2012; Liu *et al.*, 2012; Yang *et al.*, 2013; Holding and Allen, 2015; Levanon
76 *et al.*, 2016]. However, only a few studies have compared model simulations with real-world
77 measurements over an entire lunar cycle [Abarca *et al.*, 2013; Heiss and Michael, 2014]. These
78 studies have demonstrated that tides create complex flow patterns.
79

80 Coastal forcing can also lead to significant changes in coastal geomorphology, e.g. migration of
81 sandbars or coastal erosion [Anthony, 2013]. Complex fluid and sediment interactions, such as
82 interactions between breaking waves, wave run-up and run-down, and groundwater flow in the
83 swash zone, strongly determine the accretion or erosion rate of a coastal beach [Bakhtyar *et al.*,
84 2009]. The resulting cross-shore and alongshore morphological evolution of a coast can have
85 large influences on the extent of SWI and LSI [Ataie-Ashtiani *et al.*, 2013; Zhang *et al.*, 2016].
86

87 In this study we investigated the impact of coastal hydro- and morphodynamics on coastal
88 groundwater with geophysical measurements and model simulations during the winter of 2014-
89 2015. We have used time-lapse ERT to perform automated measurements of changes in the
90 fresh-salt groundwater distribution in a mega-nourishment pilot called the Sand Engine, located
91 in the Netherlands [Mulder and Tonnon, 2011]. The aim of this study is to examine the impact of
92 coastal forcing on the fresh-salt groundwater distribution, to evaluate the quality of time-lapse
93 ERT as a monitoring method of LSI and SWI in coastal aquifers, and to assess the ability of a
94 variable-density groundwater and coupled salt transport model to simulate the observed
95 variability and change. For the evaluation of time-lapse ERT as a monitoring method, we have
96 performed sensitivity analysis and synthetic modeling as described in Henderson *et al.* [2010].
97

98 The most innovative aspect of this study is that we combined intensive monitoring of SWI and
99 LSI with detailed model simulations over a period of several months. The morphodynamic
100 environment of the measurement area resulted in the measurement of the impact of tides, storm
101 surges and coastal geomorphological changes on the fresh-salt groundwater distribution in a real-
102 world coastal aquifer. The paper first briefly describes the study site and monitoring setup, and
103 then provides an overview of the key results from time-lapse ERT measurement. Next, the model

104 setup, calibration and results are described, evaluated and discussed, emphasizing on the quality
105 of ERT measurements for the monitoring of SWI processes.

106 **2 Data and Methods**

107 **2.1 Study site: the Sand Engine**

108 The Sand Engine (also called Sand Motor) is a pilot project that consists of the construction of a
109 concentrated (mega) nourishment of 21.5 million m³ sand at the Dutch coast in 2011 (Figure 2),
110 and the evaluation of this new type of nourishment with respect to current practices in the
111 Netherlands (i.e. large-scale distribution of sand). The postulated theory is that natural forces
112 (wind, waves and currents) will gradually distribute the replenished sand along the retreating
113 coast, support natural dune growth, and simultaneously limit the disturbance of local ecosystems.
114 First results confirm that the mega-nourishment led to a growth of adjacent coastal sections and
115 dunes [*de Schipper et al.*, 2016]. In addition, recent research showed that concentrated mega-
116 nourishments can lead to an increase of local fresh groundwater resources [*Huizer et al.*, 2016].
117

118 In the study area the primary source of fresh groundwater is precipitation, which was on average
119 938 mm per year in the period June 2011 until May 2016. Another important source of fresh
120 groundwater is the inflow of groundwater from the adjacent dune area Solleveld through the
121 unconfined coastal aquifer. In general this coastal aquifer consists of 15 to 25 m fine to coarse
122 sand (median grain size of 150 to 400 µm), with a few thin discontinuous clay layers, and is
123 separated from underlying aquifers by a layer of clay and peat (Figure 2). Groundwater head
124 measurements in the dunes, and previous model simulations of the area [*Huizer et al.*, 2016]
125 indicate that groundwater flows downward through this aquitard. Groundwater level
126 measurements in monitoring wells 1 to 8 (Figure 2) on the Sand Engine show no long-term
127 trend, which suggests that the initial effect of the nourishment on groundwater heads is currently
128 small or absent. However, the volume of fresh groundwater resources seems to be gradually
129 increasing in the study area, and in the remainder of this paper we have investigated the impact
130 of tides and storm surges on these resources.

131 **2.2 Resistivity imaging (ERT)**

132 Most applications of ERT are based on the analysis of contrasts in the electrical resistivity of
133 sediments or fluids to monitor processes in porous media [*Kuras et al.*, 2009]. In this case, the
134 contrasts in the electrical resistivity are primarily caused by differences in water content, and
135 groundwater salinity. The measurement of the DC resistivity is based on the injection of an
136 electrical current in the ground with multi-electrode arrays and measurement of the potential
137 differences in the other electrodes. An increase in the distance between electrodes reduces the
138 spatial resolution and enlarges the depth of investigation, while different pairs of injection
139 electrodes along the profile line allow imaging of the resistivity distribution of the subsurface.

140 **2.2.1 Measurement set-up**

141 We conducted automated time-lapse ERT measurements from 14 November 2014 10:58 until 20
142 January 2015 10:23, along an 80 m transect at the outer perimeter of the Sand Engine (Figure 2),
143 situated perpendicular to the shoreline (i.e. cross-shore direction). The surface elevation along

144 the transect varied from +1 to +3 m MSL, encompassing the local mean high water (MHW)
145 height of +1.09 m MSL at the site (Figure 3). Alongside this transect two monitoring wells (D1
146 and D2) were installed for the measurement of groundwater heads and groundwater conductivity
147 (Figure 2). This specific location was selected for three reasons: (1) the local topography was
148 relatively simple and similar along the shoreline; (2) field data and model simulations indicate
149 that the dominant groundwater flow direction was cross-shore, and therefore parallel to the
150 transect; and (3) this section of the Sand Engine was most vulnerable to LSI. The 2-D
151 measurement set-up requires a (predominantly) parallel direction of groundwater flow and LSI,
152 to avoid a misinterpretation of observed changes in the resistivity images.

153
154 For all ERT measurements the dipole-dipole configuration was implemented, which is a
155 conventional and frequently used configuration in surveys since it is sensitive to lateral changes
156 while the acquisition time is fast, something of importance in time-lapse studies. The
157 measurement set-up consisted of 160 electrodes with a constant spacing of 0.5 m between each
158 electrode. Each electrode was connected to an iron pin – located at the same position and depth
159 as the electrode – with a stainless steel wire. All electrodes were buried in a trench with a depth
160 of 0.3 to 0.5 m below surface, for public health and safety and to protect the electrodes from
161 coastal forcing and vandalism. The measurements were carried out and controlled with the MPT
162 DAS-1 Electrical Impedance Tomography System, which was placed (with all related
163 equipment) in an elevated and locked container to protect the instruments. The system was
164 connected with another buried electrical cable to the electricity network in the Argus (video
165 sampling) station, which is located in the center of the Sand Engine [Rutten *et al.*, 2017]. In
166 addition, the system was connected to the Internet with the MRD-350 industrial mobile
167 broadband (3G router), to be able to remotely monitor and control the measurements.

168
169 However, substantial coastal erosion during the measurement period (Figure 3) led to the
170 exposure segments of of the electrode array, and consequently broken electrode connections.
171 This rendered lower sections of the electrode array unusable, and therefore the number of
172 available electrodes dropped during the measurements (Figure 3): all 160 electrodes were
173 employed until 11 December 2014, 96 electrodes until 9 January 2015, and 47 electrodes until 20
174 January 2015. In order to maximize the number of measurements, the time interval between
175 measurements was reduced in accordance with the decline in electrodes. Until 23 December
176 2014 the measurements were conducted with an interval of 30 minutes, from 24 December 2014
177 to 13 January 2015 19:00 with an interval of 15 minutes, from 13 January 2015 19:00 to 20
178 January 2015 with an interval of 10 minutes. This coastal erosion also affected the measurements
179 in monitoring well D1 and D2, and reliable groundwater level and groundwater conductivity
180 measurements could only be obtained until 19 December 2014.

181 **2.2.2 Resistivity inversion**

182 All resistivity measurements were inverted with the four-dimensional (4-D) inversion algorithm
183 as described by *Kim et al.* (2009, 2013), and *Karaoulis et al.* (2011), where inversion is the
184 procedure to go from the measured data to an inverted resistivity image, also called a tomogram.
185 In this algorithm both data and model are defined in space-time coordinates, and regularizations
186 in both space and time domains are adopted to reduce inversion artifacts and to stabilize the
187 inversion. The objective function consists of three terms that are minimized in a trade-off
188 manner: data misfit, model roughness in the space domain, and model roughness in the time

189 domain [Kim *et al.*, 2009]. The minimization is expressed either in terms of the L1 norm or the
 190 L2 norm, and the selection of the norm is dependent on the behavior of the data and the inverse
 191 model parameters [Kim *et al.*, 2013].

192
 193 The inversion was conducted sequentially with five monitoring surveys or reference time steps in
 194 each inversion, and every inversion used homogeneous half-space as the starting model. The
 195 inversion model consisted of 159 columns with a constant spacing of 0.5 m, and 9 layers with a
 196 variable thickness of 0.167 to 0.833 m. All minimizations were expressed in terms of the L2
 197 norm (i.e. full least-squares minimization), and the inversion of the model roughness in the space
 198 domain was conducted with a constant Lagrangian multiplier of 0.1. In addition, negative
 199 apparent resistivities and one electrode (and related electrode combinations) with a continuously
 200 high contact resistance were excluded from the inversion. All resulting unweighted and
 201 weighted RMS errors in the inversion process remained below 1%.

202 2.2.3 Salinity-Conductivity relationship

203 For the comparison of the inverted electrical resistivities with model simulated salinities, we
 204 estimated the salinity (expressed in total dissolved solids - TDS) from the inverted bulk electrical
 205 resistivities (ρ in Ohm m) using a similar procedure as described in *Post* (2012) and *Hermans et*
 206 *al.* (2012). First the groundwater resistivity (ρ_w in Ohm m), and inversely the groundwater
 207 conductivity (σ_w in S m⁻¹), was estimated from the bulk resistivity with a variant of the classical
 208 *Waxman and Smits* (1968) model. The cation exchange capacity in this model was ignored,
 209 because the clay fraction in the upper part of the sand nourishment is negligible (Figure 2). This
 210 reduces the model to a simple linear relation:

$$211 \rho = \rho_w \cdot \frac{F}{s_w^n}; \quad \sigma = \sigma_w \cdot \frac{s_w^n}{F} \quad (1)$$

212 where F is the electrical formation factor of the sediment, s_w is the relative water saturation, and
 213 n is the saturation exponent.

214
 215
 216 The focus of this research was limited to the saturated zone, and thus s_w was constrained to a
 217 value of 1. Estimated salinities in the unsaturated zone were therefore excluded from the analysis
 218 of the effect of tides and storm surges. The formation factor was also estimated with Equation 1,
 219 i.e. equal to the ratio between the groundwater conductivity and the bulk conductivity (σ in S m⁻¹):
 220 on-site measurements of the groundwater conductivity between 14 November 2014 10:58 and
 221 11 December 2014 03:57 in monitoring well D1 (Figure 3) at a depth of -0.5 m MSL were
 222 divided by the inverted bulk conductivity at the same approximate position. Ignoring anomalous
 223 conductivities, this resulted in an average formation factor of 4.2 in this period with a standard
 224 deviation of 0.3, which is similar to literature values for coarse sand [*Friedman*, 2005; *Goes et*
 225 *al.*, 2009]. The variability in the formation factor was mainly a result of fluctuations in the on-
 226 site measured groundwater conductivity, and a gradual decline in only the inverted bulk
 227 conductivity. Possibly the water inside monitoring well D1 was more sensitive to LSI, which led
 228 to a larger response in conductivity and the absence of a (clear) falling trend.

229
 230 Groundwater salinities were estimated with the salinity-conductivity relationship as defined in
 231 the algorithm of the Practical Salinity Scale (PSS) 1978 [*Fofonoff and Millard Jr.*, 1983]. This
 232 so-called Practical Salinity S_p is a dimensionless measure of salinity, which is defined in terms of

233 the ratio with the conductivity of standard seawater ($S_p = 35$) at a temperature of 15 °C, and at
234 atmospheric pressure. The calculation of S_p is dependent on the electrical conductivity, the
235 temperature and (water) pressure at depth of the measurement [IOC *et al.*, 2010]. Temperatures
236 were estimated with measurements in monitoring well 2 at a depth of -0.2 m MSL (Figure 2),
237 which dropped from 13.8 °C on 14 November 2014 to 10.6 °C on 20 January 2015. Deviations
238 from atmospheric pressure were ignored in the calculations, because the observed variations in
239 atmospheric pressure have negligible effects on the S_p . The PSS 1978 is only defined for
240 salinities in the range $2 < S_p < 42$. Consequently, for salinities between 0 and 2 the extension of
241 the PSS 1978 as defined by Hill *et al.* (1986) was adopted. The dimensionless values for S_p were
242 converted to salinities in g TDS L⁻¹, with the relationship between the chloride concentration and
243 the Practical Salinity as described in Millero *et al.* (2008).

244 **2.3 Variable density groundwater flow model**

245 For the analysis of the observed changes in groundwater head and salinity in the fresh-salt
246 groundwater mixing zone, we developed a 2-D variable-density groundwater model with a
247 horizontal spacing of 0.2 m and vertical spacing of 0.2 m. Variable-density saturated
248 groundwater flow and coupled salinity transport were simulated with the computer code
249 SEAWAT [Langevin *et al.*, 2008]. The governing flow and solute transport equations in
250 SEAWAT are coupled and solved with a cell-centered finite difference approximation.
251 Numerous studies have used this model code to simulate variably-density, transient groundwater
252 flow in coastal environments [Mao *et al.*, 2006; Robinson *et al.*, 2007b; Heiss and Michael,
253 2014; Pauw *et al.*, 2014]. Pressure heads and saturation levels in the unsaturated zone will have
254 an important impact on infiltration rates, however in this research we have focused on processes
255 in the saturated zone. In the simulations we have assumed that the infiltration of freshwater by
256 precipitation and seawater by LSI occur instantaneously. We believe this choice is justified
257 because of the high infiltration rates of the coarse sand, and the relatively shallow unsaturated
258 zone along the measurement transect (maximum 2 m).

259

260 The groundwater flow model was situated perpendicular to the shoreline, alongside the ERT
261 measurement transect (Figure 2). Based on four boreholes with a depth of 20 m below surface,
262 situated 7 to 400 m from the model transect, we modeled two aquifers and one aquitard (see
263 cross section in Figure 2). The aquifers contain fine-grained to medium coarse-grained sand and
264 occasionally shells, and the aquitard consist of sandy clay to clay.

265 **2.3.1 Initial conditions**

266 The groundwater head and salinity distribution at the start of the time-lapse ERT measurement
267 were reconstructed with model simulations from the completion of the Sand Engine in June 2011
268 until the start of the measurements in November 2014. The initial distribution of the groundwater
269 salinity in the model was defined completely saline, i.e. equal to the average seawater salinity at
270 the site of approximately 28 g TDS L⁻¹ [Rijkswaterstaat, 2012]. In the intervening period the
271 Sand Engine experienced substantial geomorphological changes, in particular along the outer
272 perimeter of the peninsula, where the shoreline retreated approximately 200 m [de Schipper *et al.*,
273 2016]. These geomorphological changes of the Sand Engine were monitored with monthly to
274 bimonthly topographic surveys (including bathymetry) as part of an intensive monitoring
275 program. Dependent on the monitoring frequency and the extent of morphological change we

276 have updated the surface elevation every one to three months in the model by sequential grid
 277 regenerations. For the extent of the morphological change we used this criterion for the exclusion
 278 of topographic surveys: the maximum (horizontal) shift in the topography, above the mean neap
 279 tide height (+0.86 m MSL) and below the maximum run-up height (in the concerning period),
 280 should be smaller than 10 m. The excluded surveys (8 out of a total of 30 surveys) were either
 281 conducted in the summer season (fewer storm surges), or surveys that were conducted quickly
 282 after another (e.g. twice in one month).

283 **2.3.2 Boundary conditions**

284 Sea-level fluctuations were based on high frequency (10-minute time interval) tide gauge
 285 measurements (also called Still Water Level: SWL) in the harbors of Scheveningen and Hoek
 286 van Holland, which are located 7.5 km north and 9.3 km south from the study site. Based on the
 287 position of the study site we used an averaged time-series of both measurement sites as an
 288 estimate of the local sea-level fluctuations. This approximation was corroborated with a
 289 comparison to short-term on-site sea-level measurements between 17 September and 23 October
 290 2014, which revealed an absolute mean error of 0.06 m and a RMSE of 0.075 m. In the model
 291 simulations only sea-level fluctuations larger than 2 cm were incorporated, which resulted in
 292 stress periods with a variable duration of 10 to 190 minutes.

293
 294 Based on the sea-level and the topography, the inundation extent was determined for every stress
 295 period, and modeled as ‘General Head (head-dependent) Boundaries and Drains’ as described in
 296 *Mulligan et al.*, (2011). All model layers in the phreatic aquifer (Figure 2) were defined
 297 convertible (saturated thickness) and rewettable with a wetting threshold of 0.01 m [*McDonald et*
 298 *al.*, 1992]. Despite this relatively small wetting threshold, and detail in the simulation of the sea-
 299 level fluctuations, not all model cells were reactivated in every stress period unless an additional
 300 infiltration rate was added to the simulations. This deficiency was only observed for sea-levels
 301 that were larger than the MHW height. Therefore, to ensure a reactivation of all inundated model
 302 cells, an additional infiltration of 0.008 m per minute of seawater was added to the area of
 303 inundation for sea-levels larger than the MHW height. The adopted infiltration rate was the
 304 lowest rate that led to a reactivation of all inundated model cells, and this rate equaled the
 305 drainable volume of two model layers over a 10-minute period.

306
 307 Besides this simulation of the SWL (model scenario S1), two additional model scenarios (S2 and
 308 S3) with estimations of respectively the wave set-up height and the wave run-up height at the site
 309 were implemented to study and improve the resemblance of the simulations with reality (Figure
 310 1). Wave set-up is defined as the local rise of the mean seawater level (with respect to SWL),
 311 caused by wave breaking. Wave run-up is defined as the maximum level of wave up-rush on the
 312 beach (with respect to SWL), which is only exceeded by 2% of run-up events. The wave set-up
 313 height $\langle \eta \rangle$ and wave run-up height R_2 in every stress period were estimated with general
 314 empirical expressions [*Stockdon et al.*, 2006]:

$$315 \quad \langle \eta \rangle = 0.35 \beta_f (H_0 L_0)^{1/2} \quad (2)$$

$$317 \quad R_2 = 1.1 \left(0.35 \beta_f (H_0 L_0)^{1/2} + \frac{[H_0 L_0 (0.563 \beta_f^2 + 0.004)]^{1/2}}{2} \right) \quad (3)$$

318

319 where H_0 is the deep water significant wave height, L_0 is the deep water wave length, and β_f is
320 the foreshore beach slope. The significant wave height and wave length were estimated with
321 measurements at the ‘Euro platform’ of the Ministry of Infrastructure and the Environment
322 (Rijkswaterstaat), which is located 50 km southwest from the study site (Figure 4).

323

324 Wave set-up (S2) was modeled similarly to the observed sea-level fluctuations (SWL), and wave
325 run-up (S3) as the combination of wave set-up and wave up-rush (Figure 1). Non-linear effects
326 of wave set-up on the surface water level were not included, because possible seawater
327 circulations through the aquifer will probably have a small to negligible effect on the fresh-salt
328 groundwater distribution. Wave up-rush was modeled as an infiltration of seawater, between the
329 wave set-up height $\langle \eta \rangle$ and the wave run-up height R_2 . The infiltrated volume of seawater at
330 the wave set-up height $\langle \eta \rangle$ was estimated – in every stress period – as the drainable storage
331 (determined by specific yield) between SWL and $\langle \eta \rangle$. Above the wave set-up height $\langle \eta \rangle$
332 this infiltration volume was reduced linearly to a value of 10 percent at the wave run-up
333 height R_2 . The value of 10 percent is a best guess that was based on the number of run-up events
334 that reach the run-up height R_2 (generally between 1 and 3 events in 10 minutes), the average
335 infiltrated volume at the wave set-up height $\langle \eta \rangle$ (0.013 m between June 2011 and 20 January
336 2015), and the assumption that at least 0.001 m infiltrates during every run-up event.

337

338 The inland boundary of the model was simulated as a constant groundwater head and constant
339 concentration boundary, where the vertical distribution and change of the groundwater head and
340 salinity in the boundary were estimated with a separate 1-D groundwater flow model. This 1-D
341 model consisted of the same hydrogeological properties as the calibrated 2-D model (Table 1),
342 groundwater recharge, and the local saline groundwater head (monitoring well 8). Based on
343 groundwater level measurements in monitoring wells 2, 4 and 8 and the local topography, we
344 assumed that the change in groundwater salinity was predominantly determined by groundwater
345 recharge. The local groundwater head was assigned to the bottommost model layer and defined
346 as a variable head, equal to the daily moving average of the measured groundwater head in
347 monitoring well 8 for the period 1 June 2014 to 20 January 2015 (Figure 2). In the preceding
348 period, we have implemented the average groundwater head. The salinity in this bottommost
349 layer was set equal to average seawater salinity.

350 Hourly measurements of precipitation and reference crop evapotranspiration at a measurement
351 station in Hoek van Holland were used to estimate groundwater recharge. The hourly
352 groundwater recharge was linearly distributed over smaller-sized stress periods. For the
353 estimation of the potential soil evaporation we used crop coefficients for bare or sandy soil [*de*
354 *Bruin*, 1987; *Meinardi*, 1994; *Spijksma et al.*, 1995]: 0.6 for the summer (April – September),
355 and 0.9 for the winter (October – March). Monthly precipitation and potential soil evaporation
356 were subtracted, in order to generate monthly estimates of the fraction of the hourly precipitation
357 that reaches the groundwater level. It is important to note that this approach might lead to an
358 overestimation of soil evaporation in months with prolonged dry periods, which will mainly
359 affect the summer season and to a lesser extent the winter season.

360 **2.3.3 Model calibration**

361 The groundwater model was calibrated with measurements of the groundwater head in multi-
362 level monitoring well 2, which is situated alongside the 2-D model (Figure 2). This monitoring

363 well contained two well screens, situated in separate aquifers (see cross-section in Figure 2). The
364 calibration was performed with model scenarios S1, S2 and S3 (respectively SWL, wave set-up,
365 and, wave run-up), for measurements from 1 May 2014 until the start of the scenario simulations
366 on 21 October 2014. The calibration strategy consisted of extensive sensitivity analyses, manual
367 model parameter calibration, and comparisons of measured and simulated groundwater heads for
368 the calibration period. In this strategy we have adopted two calibration criteria: the error between
369 the measured and simulated groundwater head should be smaller than the observed variation in
370 groundwater level (average standard deviation is 0.1 m in the calibration period), and the
371 simulated groundwater head should correlate with the observed fluctuation pattern.

372
373 The parameter calibration comprised of the manual adjustment of a selection of the most
374 sensitive model parameters: (horizontal and vertical) hydraulic conductivity, storage coefficients,
375 and (longitudinal and transverse) dispersivity. These adjustments consisted of small incremental
376 changes from an initial best guess, which was based on previous model simulations in the same
377 area [Huizer *et al.*, 2016]. Other parameters such as groundwater recharge were based on
378 measurements, and were excluded from the calibration. The longitudinal and transversal
379 dispersivity were adapted in agreement with the observed mixing zone thickness. The calibrated
380 set of model parameters is shown in Table 1.

381 **2.3.4 Model scenarios**

382 As described in section 2.3.2, the observed SWL, estimated wave set-up, and estimated wave
383 run-up were implemented in three separate model scenarios (S1, S2 and S3), to analyze the
384 reproducibility of the observed LSI and SWI processes in the ERT measurements. These model
385 scenarios S1, S2 and S3 were executed for the initialization period of 1 June 2011 (completion
386 Sand Engine) to 21 October 2014, and the study period of the 21 October 2014 to the end of the
387 ERT measurements on 20 January 2015. The simulations were started before the ERT
388 measurements to incorporate the storm surge that occurred between 21 October 2014 16:00 until
389 22 October 09:00 (significant offshore wave height of 4 to 5.4 m, and offshore wave period of
390 6.3 to 7.2 s). This storm surge led to the inundation of the entire measurement transect, as
391 indicated with the highest measured SWL on the 22 October 2014 in Figure 5. This was the most
392 intensive storm at the Sand Engine since 6 December 2013, which led to the highest seawater
393 level and consequently the most extensive LSI of the measurement period. Other storms that
394 occurred during the measurement period were on 11 December 2014 (significant offshore wave
395 height of 3 to 4 m, and offshore wave period of 5.5 to 6.5 s) and on 11 January 2015 (significant
396 offshore wave height of 3.5 to 4.2 m, and offshore wave period of 5.8 to 6.7 s), and the highest
397 measured seawater levels during these storms are also indicated in Figure 5.

398
399 Coastal forcing - and the earlier mentioned storm surges in particular - led to substantial
400 morphological changes at the Sand Engine in the measurement period, as illustrated in Figure 5.
401 This morphological change is based on two extensive topographic (including bathymetry)
402 surveys that were conducted on the Sand Engine between 27 October 2014 and 1 November
403 2014, and between 17 and 24 January 2015. Each survey produced a large collection of height
404 measurements that were spatially interpolated to obtain an estimation of the surface elevation
405 along the model transect (Figure 5). The disparity between these surface elevations shows the
406 retreat of the shoreline at the site during the surveys. In order to obtain an optimal
407 correspondence in the actual and the modeled topography, the horizontal average of both surface

408 elevations was used as an estimation of the intermediate elevation along the model transect from
409 12 to 31 December 2015. Before and after this period we have adopted interpolations of the two
410 topographic measurements (see dashed line in Figure 5).

411

412 In order to study the effect of groundwater recharge on the salinity distribution in more detail,
413 model scenario S3 was also simulated without groundwater recharge. This simulation was only
414 executed for the study period after the calibration (21 October 2014 to 20 January 2015), and
415 preceding simulations of model scenario S3 were used as initial conditions.

416 **3 Results**

417 **3.1 Groundwater head**

418 In most of the calibration period the simulated groundwater head in the model scenarios closely
419 resemble the observed fluctuation pattern, substantiating that the groundwater model accurately
420 describes the course of the groundwater level and groundwater flow in the study site (Figure 6).
421 The absolute mean error between the measured and simulated groundwater head of model
422 scenario S1, S2 and S3 is respectively 0.06, 0.05 and 0.05 m in the phreatic aquifer (RMSE 0.07,
423 0.06 and 0.05 m), and respectively 0.13, 0.12 and 0.10 m in the bottom aquifer (RMSE 0.17,
424 0.15 and 0.13 m). Wave set-up (S2) and in particular wave run-up (S3) results in larger LSI and
425 consequently higher groundwater levels. Overall, the observed fluctuation in groundwater head
426 can to a large extent be explained by variations in sea-level (spring tide – neap tide cycle),
427 coastal geomorphology, groundwater recharge, and groundwater flow across the inland model
428 boundary. The initial deviation of the groundwater head of approximately 0.20 in the
429 bottommost aquifer – in contrast with the resemblance in the upper aquifer - is probably caused
430 by underestimations in the inflow of groundwater across the inland model boundary in the
431 previous period, possibly in combination with geologic differences.

432

433 Focusing on the effect of tides and storm surges, Figure 6 shows that for most LSI instances
434 (indicated with black arrows) the simulated increase in groundwater head is similar to the
435 measurements (e.g. on 9 and 24 September), while in some instances the model overestimates
436 the increase in groundwater head (e.g. on 14 and 30 July). Probably the primary cause for this
437 contrast are mismatches between the actual and modeled topography, which is a consequence of
438 continued morphological changes between the bimonthly topographic surveys. For example,
439 photographs of the Sand Engine from the Argus (video sampling) station indicate that a sand bar
440 developed in the intertidal zone, after the storm surge on 9 July 2014 (Figure 4), and this sand
441 bar could have dampened the extent of the LSI on 14 and 30 July.

442

443 As for precipitation, Figure 6 shows that precipitation led to negligible to small rises – often in
444 the order of centimeters - in the measured groundwater level, as for example during relatively
445 high rainfall events on 27 May (17.7 mm in 15 hours) and 28 July (16.8 mm in 11 hours).
446 Because the measured precipitation was probably generally close to reality, this indicates that the
447 volume of groundwater recharge was substantially reduced due to evaporation and storage. In
448 most instances the simulated response to precipitation was similar to the measured response,
449 however in some instances (e.g. the period of high rainfall between 13 and 25 August) the
450 simulated change in groundwater head appeared to large when compared with measurements.

451 This suggests that either the simulated evaporation in this period was underestimated, or that the
452 volume of precipitation stored in the unsaturated zone was larger than anticipated.

453

454 The performance of the calibrated model was examined with observations of the groundwater
455 level from 7 November to 19 December 2014, taken in monitoring well D1 and D2 (Figure 7).
456 These observations were situated near the local MHW height of +1.09 m MSL and were
457 therefore more exposed to sea-level fluctuations in comparison with monitoring well 2. The
458 similarity in the observed and simulated groundwater head in this period confirms the reliability
459 of the calibrated model at different distances from the local MHW height. The absolute mean
460 error between the measured and simulated groundwater head of model scenario S1, S2 and S3 is
461 respectively 0.142, 0.138 and 0.135 m for monitoring well D1 (RMSE 0.19, 0.18 and 0.17 m),
462 and respectively 0.14, 0.13 and 0.11 m for monitoring well D2 (RMSE 0.20, 0.18 and 0.15 m).

463

464 During the first four weeks (7 November to 5 December) the weather conditions were generally
465 calm with low wave heights (Figure 4), in contrast with the stormy conditions in the last two
466 weeks (5 to 19 December). This resulted in fewer and less extensive inundations in the period
467 before 5 December, and consequently smaller variations in groundwater head, and this contrast is
468 captured in both the measured and simulated groundwater head. However, in some periods the
469 simulated and measured groundwater head diverge, as for example between 17 and 22
470 November. Photographs of the study site from the Argus (video sampling) station indicate that
471 this mismatch is probably caused by a sand bar, which (slowly) developed in the intertidal zone
472 in this period, and this shortened or dampened the extent of inundations.

473

474 In addition, the figure shows that in many instances the response of the groundwater head to LSI
475 is underestimated. However, comparisons of the model scenarios (Figure 7) suggest that the
476 incorporation of wave run-up led to a small improvement in the simulation of the response of the
477 groundwater level to coastal hydro- and morphodynamics. In particular in scenario S1 (SWL) the
478 model seems to underestimate short-term fluctuations in groundwater level, but the incorporation
479 of wave run-up in model scenario S3 led to additional inundation height of 0.1 to 0.7 m.

480 **3.2 Land-surface inundation (LSI)**

481 For the analysis of the frequency and extent of LSI during the measurement period, observed
482 instances of LSI along the ERT measurement transect were compared with the simulated LSI in
483 model scenario S1 (SWL) and S3 (wave run-up; Figure 8). In both measurements and model
484 simulations we have defined the maximum extent of LSI (defined with respect to the seaward
485 boundary of the electrode array) on the basis of the first substantial deviation in the resistivity or
486 salinity (at least 100%) in the upper layers of the phreatic aquifer.

487

488 Variations in the extent of LSI (Figure 8) show that LSI are not only dependent on the sea-level,
489 but also on the storm intensity, and (changes in) the local topography (i.e. surface elevation and
490 morphology). Changes in the storm intensity can lead to substantial variations in wave run-up,
491 and therefore to an extension of LSI in instances with equal sea-levels. The simulations confirm
492 the importance of wave run-up by showing that the incorporation of wave run-up reduces the
493 underestimation in the level of LSI and lowers the error between the measured and simulated
494 extent of LSI in all instances. However, variations in the local topography, due to the continued
495 retreat of the shoreline (Figure 5), can also lead to substantial shifts in the area of inundation.

496 **3.3 Groundwater salinity**

497 The inverted time series of resistivity images of 14 November 2014 to 20 January 2015 were
498 converted to salinity with the procedure that was described in Section 2.2.3. In the presentation
499 and discussion of the results we have concentrated on these salinities to be able to differentiate
500 between fresh, brackish and salt groundwater, to improve the connection of changes in salinity
501 with LSI or other processes, and to perform side-by-side comparisons with the model simulated
502 salinities. But first this time series of interpreted groundwater salinities was used to investigate
503 the effect of coastal hydro- and morphodynamics on the fresh-salt groundwater distribution. In
504 this study we have focused on the change in groundwater salinity between the groundwater level
505 and a depth of -1 m MSL, because the aim of this study lied on fresh groundwater resources and
506 this depth range encompasses most of the observed changes in the fresh-salt groundwater mixing
507 zone, and because the ERT data were most sensitive and therefore reliable near the surface (see
508 Appendix A).
509

510 The observed changes in groundwater salinity in the measurement period show that in most
511 instances an increase in salinity coincides with tides and storm surges, and that the impact varies
512 with the extent of the inundation. This is illustrated in Figure 9, with the (average) maximum
513 increase in salinity and the (average) total increase in salinity during LSI between 14 November
514 and 11 December, for LSI with sea-levels larger or equal to +0.86 m MSL (Mean High Water
515 Neap: MHWN), +1.09 m MSL (MHW), and +1.28 m MSL (MHWS). Decreases in salinity along
516 the measurement transect are predominantly caused by falling groundwater levels (frequently as
517 a consequence of LSI), and to a lesser extent by (high) rainfall events (Figure 10). However
518 some of the (small) changes in the measured salinity cannot be explained by LSI and recharge.
519 Possible causes for these are small fluctuations in the electrical resistivity, measurement errors
520 (related to disconnection of electrodes or rapid changes in resistivity), and changes in moisture
521 content in the unsaturated zone.
522

523 For the examination of particular effects of LSI (e.g. wave run-up and recharge) on the fresh-salt
524 groundwater distribution, we compared measured and simulated changes in groundwater salinity.
525 The comparison of the change in salinity was conducted in two respects: first in relation to the
526 change in groundwater salinity (Figure 10), and second in time (Figure 11 and Figure 12) with
527 respect to the salinity distribution on the 14 November 2014 11:00 (start of measurements).
528 Changes in the length of the electrode array (Figure 3) were adopted in the comparison with
529 model simulations, and only sections with reliable measurements were compared.
530

531 The overall resemblance between the measured and simulated change in groundwater salinity
532 demonstrates – in particular for model scenario S3 – that the changes in groundwater salinity
533 along the measurement transect are primarily determined by sea-level fluctuations and associated
534 groundwater flow (Figure 10 and Figure 11). In addition, the contrast in the reproducibility of the
535 observed phenomena between model scenario S1 (SWL), S2 (wave set-up), and S3 (wave run-
536 up) substantiates the importance of a reliable estimation of LSI, and in particular wave run-up.
537

538 Groundwater recharge has a small effect on the groundwater salinity in the measurement period
539 (see Figure 12). Many differences in the measured and simulated salinity are probably caused by
540 underestimations in the extent of LSI, e.g. the effect of inundations between 14 and 20
541 November, and between 20 and 24 December is underestimated (Figure 8). Other possible

542 causes for differences between measured and simulated salinities are related to errors in the
543 conversion of the electrical resistivity to groundwater salinity, underestimations in the fluctuation
544 in the groundwater level (see Figure 7), or changes in measured resistivity that are related to
545 moisture content.

546
547 Comparisons of the absolute groundwater salinity in measurements and simulations shows that
548 the general pattern matches, with increases in salinity due to inundations and a small fresh to
549 brackish groundwater lens on the landward side (Figure 13). The complete time-series of the
550 measurements and simulations is included as supplementary information. But some groundwater
551 salinities appear to be underestimated in the model simulations or overestimated in the converted
552 salinities. Conversely, the groundwater salinity at the seaward side appears to be higher in the
553 simulations. These differences are probably caused by the inversion (smoothing and artifacts, see
554 Appendix A), errors in the conversion of the resistivity to groundwater salinity, errors in the
555 initial salinity distribution, or mismatches in the salinization of the coastal aquifer during LSI.

556 **4 Discussion**

557 **4.1 Imaging groundwater salinity with ERT**

558 The time-lapse ERT measurement yielded a time-series of 2-D images of electrical resistivities.
559 For the visualization of changes in the fresh-salt groundwater distribution, and for the
560 comparison with model simulations, these resistivities (inverse is conductivity) were converted
561 to groundwater salinities with the Practical Salinity Scale (PSS) of 1978. The salinity-
562 conductivity relationship in the PSS-1978 is determined by laboratory experiments on (diluted)
563 standard seawater, and is therefore only applicable to water with a similar composition of major
564 ions (viz. Na^+ , K^+ , Mg^{2+} , Ca^{2+} , Cl^- , HCO_3^- , SO_4^{2-}) as standard seawater. Groundwater salinities at
565 the study site are predominantly a result of the mixing of seawater and rainwater, and will satisfy
566 this requirement to a large extent. However, variations in the chemical composition will probably
567 occur at low salinities (smaller than 2 g TDS L^{-1}), because of the (relatively small) inflow of
568 coastal groundwater and the formation of ions – in particular bicarbonate (HCO_3^-) – by chemical
569 processes. In addition, small errors or variations in the electrical formation factor can result in
570 substantial deviations in the determination of the groundwater conductivities.

571
572 This time-series of estimated groundwater salinities, and accordingly time-lapse ERT, provided
573 us the instruments to effectively investigate the impact of coastal hydro- and morphodynamics
574 and precipitation on coastal groundwater. The 2-D images contained detailed information on the
575 extent of LSI, and on the change in the fresh-salt groundwater distribution over time. In
576 particular the ability to perform (automated) measurements in multiple dimensions for a period
577 of two months was a benefit of the time-lapse ERT. For example, with this method we were able
578 to delineate the extent of multiple inundations with relative accuracy, and coincidentally observe
579 the (2-D) impact on the fresh-salt groundwater distribution. However, an aspect that occasionally
580 led to small anomalies is related to the duration of each individual measurement, which varied
581 between 10 to 30 minutes. Rapid changes in groundwater salinity and saturation levels during
582 individual measurements caused local anomalies in the electrical resistivity.

583

584 It should be noted that inversion of resistivity images often results in non-unique solutions of the
585 electrical resistivity, and that the resolution of inverted images decreases with depth. Generally a
586 decrease in resolution leads to a larger deviation from the actual or earth resistivity and a
587 stronger effect of the starting model and chosen regularization criteria on the acquired data.
588 Inundations of the electrode array can also lead to a reduction in the resolution, because the
589 highly conductive surface-water layer causes a preferential flow of the electrical current
590 [Henderson *et al.*, 2010]. This was anticipated in this study and therefore we have focused on
591 data that was acquired close to surface, between the groundwater level and a depth of -1 m MSL
592 as described in section 3.3. Potential poor resolutions in inundated segments of the electrode
593 would only be temporary, and the shallow fresh or brackish groundwater lens in these segments
594 would probably become completely saline. In addition, the reliability of the inversion process
595 was substantiated by low RMS errors (smaller than 1%).

596 **4.2 SWI processes due to tides and storm surges**

597 The similarity of the measured and simulated groundwater head, extent of LSI, and change in
598 groundwater salinity proves that reliable simulations of the fluctuation of the groundwater head
599 in complex dynamic coastal environments can be conducted with the adopted simulation
600 methodology. With detailed information on fluctuations in sea-level, topography, and
601 precipitation it was possible to relatively accurately reproduce short and long-term variations in
602 LSI and groundwater salinity with the calibrated variable-density groundwater model. Here, the
603 incorporation of wave set-up and especially wave run-up in the simulations led to a substantial
604 improvement in the estimation of the extent of LSI and SWI. This suggests that in areas with
605 gently sloping beach profiles the extent of inundation could be underestimated when wave run-
606 up is neglected, especially during storm surges.

607
608 An important cause of the observed differences between measurement and simulations is
609 probably related to the morphological evolution – between the monthly to bimonthly topographic
610 surveys – that was not incorporated in the simulations. This morphological evolution resulted in
611 a gradual retreat of the shoreline (often exacerbated by storm surges) and the formation of
612 sandbars along the outer perimeter of the Sand Engine, which resulted in shifts of the inundated
613 area. These sandbars could have led to a shift in the location where waves break and reduced
614 wave run-up, and (partially) blocked the flow of seawater, especially when sandbars were
615 connected along the shoreline. Thus, small morphological changes can lead to substantial
616 changes in the area of inundation and wave run-up, and therefore have a strong impact on fresh
617 groundwater in coastal aquifers. For the improvement of simulations of groundwater salinity in
618 such dynamic coastal conditions it is necessary to incorporate more information on the
619 morphological change during storm surges. Thus, for accurate and detailed delineations of the
620 groundwater head and salinity in local dynamic coastal environments, it is recommended to
621 monitor the local topography frequently or to perform accurate morphological simulations.

622
623 In general the simulated fresh-salt groundwater distribution matches the observed patterns in the
624 time-lapse ERT images. These are patterns such as the observed development of a small fresh to
625 brackish groundwater lens after the intensive storm in the night of 21 to 22 October 2014, and
626 the gradual salinization of the aquifer due to repeated LSI. Deviations in absolute groundwater
627 salinities are probably primarily caused by a combination of errors in the inversion (e.g. over
628 smoothing and inversion artifacts, see Appendix A), errors in the conversion of electrical

629 conductivities to groundwater salinities, errors in the wave set-up and wave run-up height and
630 related LSI and SWI during storm surges, and errors in the simulated fresh-salt groundwater
631 distribution in the period previous to the measurements. To differentiate the contribution of each
632 of these factors and to improve simulations in these local dynamic coastal environments it is
633 recommended to perform more extensive measurements of the groundwater salinity. In addition,
634 wave set-up and wave run-up height was estimated with empirical run-up formulas, where the
635 infiltration of seawater by wave run-up was roughly estimated. This approach generally
636 improves the simulation of SWI processes in these environments, but refinements in the
637 prediction of the extent of LSI and the infiltrated volume of seawater can lead to further
638 substantial advances. For example, the incorporation of unsaturated zone processes in the
639 approach could improve the estimation of the volume of seawater that infiltrates during wave
640 run-up, because the infiltration is probably very sensitive to the saturation level.

641 **5 Conclusions**

642 The measurements show that time-lapse ERT can be a valuable and promising technique for the
643 measurement of temporal and spatial changes in groundwater salinity in dynamic coastal
644 environments. ERT can especially be effective in the measurement of rapid processes such as the
645 effects of saltwater overwash and intrusion during and after storm surges. The observed changes
646 in salinity due to groundwater recharge, tidal dynamics, and storm surges could to a large extent
647 be simulated by a variable-density groundwater model, suggesting that given a thorough
648 understanding of the (local) system, groundwater models can be used to make predictions of the
649 effects of tides and storm surges. However, an accurate numerical simulation of the effect of LSI
650 in (topography-limited) dynamic coastal environments, and especially during storm surges,
651 requires detailed information about morphological changes along the coastline and reliable
652 estimates of the extent of wave run-up.

653 **Appendix A: Synthetic modeling**

654 The resolution of the inverted resistivity images and potential inversion artifacts was evaluated
655 with a synthetic modeling exercise, consisting of the inversion of simplified hypothetical
656 resistivity images [Henderson *et al.*, 2010]. In this study two hypothetical cases with a shallow
657 fresh groundwater lens – representative of the conditions at the study site – were created with a
658 2-D groundwater model: case 1 with a sea-level height equal to MHW (1.09 m MSL), and case 2
659 with an LSI (1.1 to 2.2 m MSL) of the fresh groundwater lens (Table A1).

660
661 This 2-D model contained the same hydrogeological properties and model parameters as the
662 calibrated model, as described in section 2.3.3. The implemented model grid was identical to the
663 tomogram: 159 columns with a constant spacing of 0.5 m, 28 layers with a constant thickness of
664 0.167 m, and a surface elevation that consists of the 160 measured electrode elevations
665 (incorporated as model nodes). The groundwater salinities in unsaturated model cells were set to
666 0.1 g TDS L⁻¹. Figure A1 shows the simulated groundwater salinity in case 1 and 2.

667
668 The generated salinity distributions were converted to resistivities with equation 1, using the
669 same formation factor as described in section 2.2.3 and the assumption that the groundwater
670 conductivity and groundwater salinity are similar. The resulting resistivities were averaged from
671 27 to 9 model layers, in accordance with the inverse model used in the time-lapse measurements:

672 159 columns with a constant spacing of 0.5 m, 9 layers with a variable thickness of 0.167 to
 673 0.833 m. In addition, we added random electrical noise of 1 mV V^{-1} to the inverse models of case
 674 1 and 2 to simulate the field data.

675

676 In order to assess the effect of the chosen minimization norm, both cases were inverted with the
 677 full least-squares inversion (minimizing in L2 norm) and the full L1 norm inversion (minimizing
 678 L1 in norm). In addition, to assess the effect of Lagrangian multipliers, both cases were also
 679 inverted with the constant multiplier of 0.1, and the automatic calculation of the multiplier that is
 680 based on the Active Constraint Balancing (ACB) technique [Yi *et al.*, 2003].

681

682 The inverted distributions of the groundwater salinity (Figure A2 and A3) closely resemble the
 683 simulated distributions (Figure A1) for both cases; the overall pattern is captured with all chosen
 684 minimization norms and with both the automatic (ACB) and constant Lagrangian multiplier. All
 685 inversions also seem to result in an over smoothing of the simulated fresh-salt groundwater
 686 mixing zone, and this effect increases with depth, parallel with the decrease in resolution.

687 In addition, Figures A2 and A3 show that most vertical features in groundwater salinity near the
 688 bottom of images are not present in the simulations, and are probably caused by the decrease in
 689 resolution with depth. These inversion artefacts occur with both the L1 and L2 minimization
 690 norms, and with the automatic and constant Lagrangian multiplier. However, the images suggest
 691 that the automatically calculated Lagrangian multiplier is more vulnerable to these inversion
 692 artefacts. For an exact comparison of the inversion methods, we have added the weighted RMS
 693 error of the inverse model and the RMS error of the groundwater salinity (inversion compared
 694 with simulation) in Table A2. The RMS error is lowest for the L2 norm minimization and the
 695 automatic Lagrangian multiplier, but the differences between the inversion methods are small.

696 **Acknowledgments and Data**

697 We thank Mike van der Werf, Marco de Kleine, and André Cinjee for their extensive support in
 698 the planning, set-up, and upkeep of the ERT measurement. This research is supported by the
 699 Dutch Technology Foundation STW, which is part of the Netherlands Organization for Scientific
 700 Research (NWO), and which is partly funded by the Ministry of Economic Affairs. This work
 701 was carried out within the Nature-driven nourishment of coastal systems (NatureCoast) program.
 702 The data used to produce the results of this paper may be obtained by contacting the
 703 corresponding author.

704 **References**

- 705 Abarca, E., H. Karam, H. F. Hemond, and C. F. Harvey (2013), Transient groundwater dynamics
 706 in a coastal aquifer: The effects of tides, the lunar cycle, and the beach profile, *Water*
 707 *Resour. Res.*, *49*(5), 2473–2488, doi:10.1002/wrcr.20075.
- 708 Anthony, E. J. (2013), Storms, shoreface morphodynamics, sand supply, and the accretion and
 709 erosion of coastal dune barriers in the southern North Sea, *Geomorphology*, *199*, 8–21,
 710 doi:10.1016/j.geomorph.2012.06.007.
- 711 Ataie-Ashtiani, B., R. E. Volker, and D. A. Lockington (1999), Tidal effects on sea water
 712 intrusion in unconfined aquifers, *J. Hydrol.*, *216*(1–2), 17–31, doi:10.1016/S0022-
 713 1694(98)00275-3.
- 714 Ataie-Ashtiani, B., A. D. Werner, C. T. Simmons, L. K. Morgan, and C. Lu (2013), How

- 715 important is the impact of land-surface inundation on seawater intrusion caused by sea-level
716 rise?, *Hydrogeol. J.*, 21(7), 1673–1677, doi:10.1007/s10040-013-1021-0.
- 717 Bakhtyar, R., D. A. Barry, L. Li, D. S. Jeng, and A. Yeganeh-Bakhtiary (2009), Modeling
718 sediment transport in the swash zone: A review, *Ocean Eng.*, 36(9–10), 767–783,
719 doi:10.1016/j.oceaneng.2009.03.003.
- 720 Beaujean, J., F. Nguyen, a. Kemna, a. Antonsson, and P. Engesgaard (2014), Calibration of
721 seawater intrusion models: Inverse parameter estimation using surface electrical resistivity
722 tomography and borehole data, *Water Resour. Res.*, 50, 6828–6849,
723 doi:10.1002/2013WR014020.
- 724 de Bruin, H. A. R. (1987), From Penman to Makkink. Evaporation and weather, in *Volume 39,*
725 *Proceedings and Information*, pp. 5–31, TNO Committee on Hydrological Research,
726 Technical Meeting 44.
- 727 Chang, S. W., T. P. Clement, M. J. Simpson, and K. K. Lee (2011), Does sea-level rise have an
728 impact on saltwater intrusion?, *Adv. Water Resour.*, 34(10), 1283–1291,
729 doi:10.1016/j.advwatres.2011.06.006.
- 730 Comte, J. C., and O. Banton (2007), Cross-validation of geo-electrical and hydrogeological
731 models to evaluate seawater intrusion in coastal aquifers, *Geophys. Res. Lett.*, 34(10), 1–5,
732 doi:10.1029/2007GL029981.
- 733 Cosgrove, W. J., and D. P. Loucks (2015), Water management: Current and future challenges
734 and research directions, *Water Resour. Res.*, 51(6), 4823–4839,
735 doi:10.1002/2014WR016869.
- 736 Ferguson, G., and T. Gleeson (2012), Vulnerability of coastal aquifers to groundwater use and
737 climate change, *Nat. Clim. Chang.*, 2(5), 342–345, doi:10.1038/nclimate1413.
- 738 Fofonoff, N. P., and R. C. Millard Jr. (1983), Algorithms for computation of fundamental
739 properties of seawater, *Unesco Tech. Pap. Mar. Sci.*, 44, 58.
- 740 de Franco, R. et al. (2009), Monitoring the saltwater intrusion by time lapse electrical resistivity
741 tomography: The Chioggia test site (Venice Lagoon, Italy), *J. Appl. Geophys.*, 69(3–4),
742 117–130, doi:10.1016/j.jappgeo.2009.08.004.
- 743 Friedman, S. P. (2005), Soil properties influencing apparent electrical conductivity: A review,
744 *Comput. Electron. Agric.*, 46(1–3 SPEC. ISS.), 45–70, doi:10.1016/j.compag.2004.11.001.
- 745 Goes, B. J. M., G. H. P. Oude Essink, R. W. Vernes, and F. Sergi (2009), Estimating the depth of
746 fresh and brackish groundwater in a predominantly saline region using geophysical and
747 hydrological methods, zeeland, the netherlands, *Near Surf. Geophys.*, 7(5–6), 401–412,
748 doi:10.3997/1873-0604.2009048.
- 749 Heiss, J. W., and H. A. Michael (2014), Saltwater-freshwater mixing dynamics in a sandy beach
750 aquifer over tidal, spring-neap, and seasonal cycles, *Water Resour. Res.*, 50(8), 6747–6766,
751 doi:10.1002/2014WR015574.Received.
- 752 Henderson, R. D., F. D. Day-Lewis, E. Abarca, C. F. Harvey, H. N. Karam, L. Liu, and J. W. J.
753 Lane (2010), Marine electrical resistivity imaging of submarine groundwater discharge:
754 sensitivity analysis and application in Waquoit Bay, Massachusetts, USA, *Hydrogeol. J.*,
755 18(1), 173–185, doi:10.1007/s10040-009-0498-z.
- 756 Herckenrath, D., C. D. Langevin, and J. Doherty (2011), Predictive uncertainty analysis of a
757 saltwater intrusion model using null-space Monte Carlo, *Water Resour. Res.*, 47(5),
758 W05504, doi:10.1029/2010WR009342.
- 759 Hermans, T., A. Vandenbohede, L. Lebbe, R. Martin, A. Kemna, J. Beaujean, and F. Nguyen
760 (2012), Imaging artificial salt water infiltration using electrical resistivity tomography

- 761 constrained by geostatistical data, *J. Hydrol.*, 438–439, 168–180,
762 doi:10.1016/j.jhydrol.2012.03.021.
- 763 Hill, K. D., T. M. Dauphinee, and D. J. Woods (1986), The extension of the Practical Salinity
764 Scale 1978 to low salinities, *IEEE J. Ocean. Eng.*, 11(1), 1–4,
765 doi:10.1109/JOE.1986.1145154.
- 766 Holding, S., and D. M. Allen (2015), From days to decades: numerical modelling of freshwater
767 lens response to climate change stressors on small low-lying islands, *Hydrol. Earth Syst.
768 Sci.*, 19(2), 933–949, doi:10.5194/hess-19-933-2015.
- 769 Huizer, S., G. H. P. Oude Essink, and M. F. P. Bierkens (2016), Fresh groundwater resources in
770 a large sand replenishment, *Hydrol. Earth Syst. Sci.*, 20, 3149–3166, doi:10.5194/hess-
771 2016-5.
- 772 IOC, SCOR, and IAPSO (2010), Appendix E: Algorithm for calculating Practical Salinity, in
773 *The international thermodynamic equation of seawater - 2010; Calculation and use of
774 thermodynamic properties*, pp. 147–151, Intergovernmental Oceanographic Commission,
775 UNESCO.
- 776 Karaoulis, M. C., J.-H. Kim, and P. I. Tsourlos (2011), 4D active time constrained resistivity
777 inversion, *J. Appl. Geophys.*, 73(1), 25–34, doi:10.1016/j.jappgeo.2010.11.002.
- 778 Ketabchi, H., D. Mahmoodzadeh, B. Ataie-Ashtiani, A. D. Werner, and C. T. Simmons (2014),
779 Sea-level rise impact on fresh groundwater lenses in two-layer small islands, *Hydrol.
780 Process.*, 28(24), 5938–5953, doi:10.1002/hyp.10059.
- 781 Ketabchi, H., D. Mahmoodzadeh, B. Ataie-ashtiani, and C. T. Simmons (2016), Sea-level rise
782 impacts on seawater intrusion in coastal aquifers : Review and integration, *J. Hydrol.*, 535,
783 235–255, doi:10.1016/j.jhydrol.2016.01.083.
- 784 Khan, S. J., D. Deere, F. D. L. Leusch, A. Humpage, M. Jenkins, and D. Cunliffe (2015),
785 Extreme Weather Events: Should Drinking Water Quality Management Systems Adapt to
786 Changing Risk Profiles?, *Water Res.*, 85, 124–136, doi:10.1016/j.watres.2015.08.018.
- 787 Kim, J. H., M. J. Yi, S. G. Park, and J. G. Kim (2009), 4-D inversion of DC resistivity
788 monitoring data acquired over a dynamically changing earth model, *J. Appl. Geophys.*,
789 68(4), 522–532, doi:10.1016/j.jappgeo.2009.03.002.
- 790 Kim, J. H., R. Supper, P. Tsourlos, and M. J. Yi (2013), Four-dimensional inversion of resistivity
791 monitoring data through Lp norm minimizations, *Geophys. J. Int.*, 195(3), 1640–1656,
792 doi:10.1093/gji/ggt324.
- 793 Kuan, W. K., G. Jin, P. Xin, C. Robinson, B. Gibbes, and L. Li (2012), Tidal influence on
794 seawater intrusion in unconfined coastal aquifers, *Water Resour. Res.*, 48(2), n/a-n/a,
795 doi:10.1029/2011WR010678.
- 796 Kuras, O., J. D. Pritchard, P. I. Meldrum, J. E. Chambers, P. B. Wilkinson, R. D. Ogilvy, and G.
797 P. Wealthall (2009), Monitoring hydraulic processes with automated time-lapse electrical
798 resistivity tomography (ALERT), *Comptes Rendus - Geosci.*, 341(10–11), 868–885,
799 doi:10.1016/j.crte.2009.07.010.
- 800 Langevin, C. D., D. T. Thorne Jr., A. Dausman, M. C. Sukop, and W. Guo (2008), SEAWAT
801 version 4: A Computer Program for Simulation of Multi-Species Solute and Heat Transport,
802 in *U.S. Geological Survey Techniques and Methods Book 6, Chapter A22*, p. 39, US
803 Geological Survey, Reston, Virginia, USA.
- 804 Levanon, E., E. Shalev, Y. Yechieli, and H. Gvirtzman (2016), Fluctuations of fresh-saline water
805 interface and of water table induced by sea tides in unconfined aquifers, *Adv. Water
806 Resour.*, 96, 34–42, doi:10.1016/j.advwatres.2016.06.013.

- 807 Liu, Y., S. Shang, and X. Mao (2012), Tidal effects on groundwater dynamics in coastal aquifer
808 under different beach slopes, *J. Hydrodyn. Ser. B*, 24(1), 97–106, doi:10.1016/S1001-
809 6058(11)60223-0.
- 810 Mao, X., P. Enot, D. A. Barry, L. Li, A. Binley, and D. S. Jeng (2006), Tidal influence on
811 behaviour of a coastal aquifer adjacent to a low-relief estuary, *J. Hydrol.*, 327(1–2), 110–
812 127, doi:10.1016/j.jhydrol.2005.11.030.
- 813 McDonald, M. G., A. W. Harbaugh, B. R. Orr, and D. J. Ackerman (1992), *A method of*
814 *converting no-flow cells to variable-head cells for the U.S. Geological Survey modular*
815 *finite-difference ground-water flow model*, U.S. Geological Survey Open-File Report 91-
816 536, Reston, Virginia, USA.
- 817 McGranahan, G., D. Balk, and B. Anderson (2007), The rising tide: assessing the risks of climate
818 change and human settlements in low elevation coastal zones, *Environ. Urban.*, 19(1), 17–
819 37, doi:10.1177/0956247807076960.
- 820 Meinardi, C. R. (1994), Groundwater recharge and travel times in the sandy regions of the
821 Netherlands, Ph.D. Thesis, VU University Amsterdam, Amsterdam, The Netherlands.
- 822 Michael, H. A., C. J. Russoniello, and L. A. Byron (2013), Global assessment of vulnerability to
823 sea-level rise in topography-limited and recharge-limited coastal groundwater systems,
824 *Water Resour. Res.*, 49(4), 2228–2240, doi:10.1002/wrcr.20213.
- 825 Millero, F. J., R. Feistel, D. G. Wright, and T. J. McDougall (2008), The composition of
826 Standard Seawater and the definition of the Reference-Composition Salinity Scale, *Deep*
827 *Sea Res. Part I Oceanogr. Res. Pap.*, 55(1), 50–72, doi:10.1016/j.dsr.2007.10.001.
- 828 Morgan, L. K., and A. D. Werner (2014), Seawater intrusion vulnerability indicators for
829 freshwater lenses in strip islands, *J. Hydrol.*, 508, 322–327,
830 doi:10.1016/j.jhydrol.2013.11.002.
- 831 Morrow, F. J., M. R. Ingham, and J. A. McConchie (2010), Monitoring of tidal influences on the
832 saline interface using resistivity traversing and cross-borehole resistivity tomography, *J.*
833 *Hydrol.*, 389(1–2), 69–77, doi:10.1016/j.jhydrol.2010.05.022.
- 834 Mulder, J. P. M., and P. K. Tonnon (2011), “Sand Engine” : Background and Design of a Mega-
835 Nourishment Pilot in The Netherlands, *Coast. Eng. Proc.*, 1(32), 1–10,
836 doi:10.9753/icce.v32.management.35.
- 837 Mulligan, A. E., C. D. Langevin, and V. E. A. Post (2011), Tidal boundary conditions in
838 SEAWAT., *Ground Water*, 49(6), 866–79, doi:10.1111/j.1745-6584.2010.00788.x.
- 839 Nguyen, F., a. Kemna, a. Antonsson, P. Engesgaard, O. Kuras, R. Ogilvy, J. Gisbert, S. Jorreto,
840 and a. Pulido-Bosch (2009), Characterization of seawater intrusion using 2D electrical
841 imaging, *Near Surf. Geophys.*, 7(5–6), 377–390, doi:10.3997/1873-0604.2009025.
- 842 Nicholls, R. J. (2010), Impacts of and responses to Sea-Level Rise, in *Understanding Sea-Level*
843 *Rise and Variability*, edited by J. A. Church, P. L. Woodworth, T. Aarup, and W. W.
844 Wilson, pp. 17–51, Wiley-Blackwell.
- 845 Ogilvy, R. D. et al. (2009), Automated Monitoring of Coastal Aquifers with Electrical Resistivity
846 Tomography, *Near Surf. Geophys.*, 7(5–6), 367–375, doi:10.1007/s13398-014-0173-7.2.
- 847 Oude Essink, G. H. P., E. S. van Baaren, and P. G. B. de Louw (2010), Effects of climate change
848 on coastal groundwater systems: A modeling study in the Netherlands, *Water Resour. Res.*,
849 46(10), W00F04, doi:10.1029/2009WR008719.
- 850 Pauw, P. S., G. H. P. Oude Essink, A. Leijnse, A. Vandenbohede, J. Groen, and S. E. A. T. M.
851 van der Zee (2014), Regional scale impact of tidal forcing on groundwater flow in
852 unconfined coastal aquifers, *J. Hydrol.*, 517, 269–283, doi:10.1016/j.jhydrol.2014.05.042.

- 853 Post, V. E. A. (2012), Electrical conductivity as a proxy for groundwater density in coastal
854 aquifers, *Ground Water*, 50(5), 785–92, doi:10.1111/j.1745-6584.2011.00903.x.
- 855 Revil, A., M. Karaoulis, T. Johnson, and A. Kemna (2012), Review: Some low-frequency
856 electrical methods for subsurface characterization and monitoring in hydrogeology,
857 *Hydrogeol. J.*, 20(4), 617–658, doi:10.1007/s10040-011-0819-x.
- 858 Rijkswaterstaat (2012), Salinity in the North Sea along the coast (in Dutch), *North Sea Atlas*,
859 *Part I. Water Syst.* Available from: [http://www.noordzeeloket.nl/en/spatial-](http://www.noordzeeloket.nl/en/spatial-management/north-sea-atlas/watersysteem/zoutgehalte.aspx)
860 [management/north-sea-atlas/watersysteem/zoutgehalte.aspx](http://www.noordzeeloket.nl/en/spatial-management/north-sea-atlas/watersysteem/zoutgehalte.aspx)
- 861 Robinson, C., L. Li, and D. A. Barry (2007a), Effect of tidal forcing on a subterranean estuary,
862 *Adv. Water Resour.*, 30(4), 851–865, doi:10.1016/j.advwatres.2006.07.006.
- 863 Robinson, C., L. Li, and H. Prommer (2007b), Tide-induced recirculation across the aquifer-
864 ocean interface, *Water Resour. Res.*, 43(7), n/a-n/a, doi:10.1029/2006WR005679.
- 865 Rutten, J., S. M. de Jong, and G. Ruessink (2017), Accuracy of Nearshore Bathymetry Inverted
866 From X-Band Radar and Optical Video Data, *IEEE Trans. Geosci. Remote Sens.*, 55(2),
867 1106–1116, doi:10.1109/TGRS.2016.2619481.
- 868 de Schipper, M. A., S. de Vries, G. Ruessink, R. C. de Zeeuw, J. Rutten, C. van Gelder-Maas,
869 and M. J. F. Stive (2016), Initial spreading of a mega feeder nourishment: Observations of
870 the Sand Engine pilot project, *Coast. Eng.*, 111, 23–38,
871 doi:10.1016/j.coastaleng.2015.10.011.
- 872 Spijksma, J. F. M., A. J. Dolman, and J. M. Schouwenaars (1995), *National Research program*
873 *Dehydration: the parameterisation of the evapotranspiration of natural areas in*
874 *hydrological models (in Dutch).*
- 875 Stockdon, H. F., R. A. Holman, P. A. Howd, and A. H. Sallenger (2006), Empirical
876 parameterization of setup, swash, and runup, *Coast. Eng.*, 53(7), 573–588,
877 doi:10.1016/j.coastaleng.2005.12.005.
- 878 Vallejos, A., F. Sola, and A. Pulido-Bosch (2014), Processes Influencing Groundwater Level and
879 the Freshwater-Saltwater Interface in a Coastal Aquifer, *Water Resour. Manag.*, 29(3), 679–
880 697, doi:10.1007/s11269-014-0621-3.
- 881 Wada, Y., L. P. H. Van Beek, C. M. Van Kempen, J. W. T. M. Reckman, S. Vasak, and M. F. P.
882 Bierkens (2010), Global depletion of groundwater resources, *Geophys. Res. Lett.*, 37(20), 1–
883 5, doi:10.1029/2010GL044571.
- 884 Wada, Y., L. P. H. Van Beek, and M. F. P. Bierkens (2012), Nonsustainable groundwater
885 sustaining irrigation: A global assessment, *Water Resour. Res.*, 48(1),
886 doi:10.1029/2011WR010562.
- 887 Watson, T. A., A. D. Werner, and C. T. Simmons (2010), Transience of seawater intrusion in
888 response to sea level rise, *Water Resour. Res.*, 46(12), 1–10, doi:10.1029/2010WR009564.
- 889 Waxman, M. H., and L. J. M. Smits (1968), Electrical conductivities in oil-bearing shaly sands,
890 *Soc. Pet. Eng. J.*, 8(2), 107–122.
- 891 Webb, M. D., and K. W. F. Howard (2011), Modeling the Transient Response of Saline Intrusion
892 to Rising Sea-Levels, *Ground Water*, 49(4), 560–569, doi:10.1111/j.1745-
893 6584.2010.00758.x.
- 894 Werner, A. D., M. Bakker, V. E. A. Post, A. Vandenbohede, C. Lu, B. Ataie-Ashtiani, C. T.
895 Simmons, and D. A. Barry (2013), Seawater intrusion processes, investigation and
896 management: Recent advances and future challenges, *Adv. Water Resour.*, 51, 3–26,
897 doi:10.1016/j.advwatres.2012.03.004.
- 898 Wilson, A. M., W. S. Moore, S. B. Joye, J. L. Anderson, and C. A. Schutte (2011), Storm-driven

- 899 groundwater flow in a salt marsh, *Water Resour. Res.*, 47(2), 1–11,
900 doi:10.1029/2010WR009496.
- 901 Wong, P. P., I. J. Losada, J.-P. Gattuso, J. Hinkel, A. Khattabi, K. L. McInnes, Y. Saito, and A.
902 Sallenger (2014), Coastal systems and low-lying areas, in *Climate Change 2014: Impacts,*
903 *Adaptation, and Vulnerability. Part A: Global and Sectoral Aspects. Contribution of*
904 *Working Group II to the Fifth Assessment Report of the Intergovernmental Panel on*
905 *Climate Change*, pp. 361–409, Cambridge University Press, Cambridge, United Kingdom
906 and New York, NY, USA.
- 907 Yang, J., T. Graf, M. Herold, and T. Ptak (2013), Modelling the effects of tides and storm surges
908 on coastal aquifers using a coupled surface–subsurface approach, *J. Contam. Hydrol.*, 149,
909 61–75, doi:10.1016/j.jconhyd.2013.03.002.
- 910 Yi, M.-J., J.-H. Kim, and S.-H. Chung (2003), Enhancing the resolving power of least squares
911 inversion with active constraint balancing, *Geophysics*, 68(3), 931–941,
912 doi:10.1190/1.1581045.
- 913 Zhang, Y., L. Li, D. V. Erler, I. R. Santos, and D. A. Lockington (2016), Effect of alongshore
914 morphology on groundwater flow and solute transport in a nearshore aquifer, *Water Resour.*
915 *Res.*, 52(2), 990–1008, doi:10.1002/2014WR015716.
916
917

918 **Table 1.** Calibrated parameter values implemented in the model simulations.

Layer type	Parameter	Value
All model layers	Longitudinal dispersivity	0.02 m
	Transverse dispersivity	0.002 m
Phreatic aquifer 1: [above -9 m MSL]	Horizontal Hydraulic conductivity	36 m d ⁻¹
	Vertical Hydraulic conductivity	18 m d ⁻¹
	Specific yield	0.20
Aquitard 1: [-13 to -14 m MSL]	Horizontal Hydraulic conductivity	1.15 · 10 ⁻¹ m d ⁻¹
	Vertical Hydraulic conductivity	1.15 · 10 ⁻² m d ⁻¹
	Specific storage	2 · 10 ⁻⁴
Aquifer 1: [-9 to -13 m MSL] 2: [-14 to -17 m MSL]	Horizontal Hydraulic conductivity	36 m d ⁻¹
	Vertical Hydraulic conductivity	7.2 m d ⁻¹
	Specific storage	2 · 10 ⁻⁴

919

920 **Table A2.** Model parameters in case 1 ‘MHW’ and case 2 ‘LSI’

Model parameter	Case 1 ‘MHW’	Case 2 ‘LSI’
Groundwater recharge	1.4 mm d ⁻¹ + 0.2 g TDS L ⁻¹	0.97 μm min ⁻¹ + 0.2 g TDS L ⁻¹
Initial conditions	1.2 m MSL + 28 g TDS L ⁻¹	Output of case 1
Inland boundary	1.1 m MSL + fresh / salt groundwater interface at 0.45 m MSL	
Model period	180 days	360 minutes / 6 hours
Sea-level	1.09 m MSL + 28 g TDS L ⁻¹	1.1 to 2.2 m MSL + 28 g TDS L ⁻¹

921

922 **Table A2.** RMS error of inverse model for case 1 ‘MHW’ and case 2 ‘LSI’

Model RMS error	Case 1 ‘MHW’		Case 2 ‘LSI’	
	Inversion	Salinity	Inversion	Salinity
L1 norm minimization Automatic Lagrangian multiplier	5.8 %	5.7 g TDS L ⁻¹	5.9 %	6.4 g TDS L ⁻¹
L1 norm minimization Constant Lagrangian multiplier	7.4 %	6.5 g TDS L ⁻¹	7.0 %	6.4 g TDS L ⁻¹
L2 norm minimization Automatic Lagrangian multiplier	5.5 %	5.7 g TDS L ⁻¹	5.6 %	6.4 g TDS L ⁻¹
L2 norm minimization Constant Lagrangian multiplier	5.7 %	5.7 g TDS L ⁻¹	5.9 %	7.3 g TDS L ⁻¹

923

924

925 **Figure 1.** Illustration of coastal flow processes at the measurement site.

926 **Figure 2.** Contour map and hydrogeological cross section of the Sand Engine between 27
927 October and 1 November 2014, with the location of the monitoring wells, ERT measurement
928 transect (red line) and the groundwater model transect (black line, A – A'). The dashed line in
929 the cross section marks the bathymetry prior to the construction of the Sand Engine.

930 **Figure 3.** Cross-section of the ERT measurement transect containing the implemented
931 consecutive model surface elevations, where the wave-shading pattern indicates the erosion of
932 sand in the measurement period. The horizontal arrows and vertical black lines mark the
933 reduction of the ERT measurement transect on 12 December 2014 and 10 January 2015.

934 **Figure 4.** Measured deep water significant wave height H_0 (daily maximum) and deep water
935 wave period (daily measured) at the 'Euro platform' (50 km southwest from the study site).

936 **Figure 5.** Cross-section with the observed surface elevations at the measurement site: 27 October
937 to 1 November 2014 (black line), and 17 to 24 January 2015 (grey line). The wave-shading
938 pattern between the lines marks the erosion or accretion of sand in the intervening period. The
939 red lines mark the ERT transect and the blue dashed lines mark the three highest SWL in the
940 measurement period.

941 **Figure 6.** Measured groundwater head (gray line) in the upper well screen of monitoring well 2
942 (a) and the lower well screen of monitoring well 2 (b), with the simulated groundwater head of
943 model scenario S1 (SWL, blue line), S2 (wave set-up, green line), and S3 (wave run-up, red
944 line). The vertical grey bars mark topographic surveys on the Sand Engine, the arrows mark LSI
945 instances where the sea-level was higher than the Mean High Water Spring (MHWS) height of
946 +1.28 m MSL, and the black bars indicate the daily precipitation (in mm d^{-1}) with a maximum of
947 21 mm on 22 august 2014.

948
949 **Figure 7.** Measured groundwater head in monitoring well D1 (a) and D2 (b), and simulated
950 groundwater head in model scenario S1 (SWL, blue line), S2 (wave set-up, green line), and S3
951 (wave run-up, red line).

952
953 **Figure 8.** Maximum extent of LSI [m] along transect with respect to seaward boundary of the
954 ERT measurement, for model scenario S1 (SWL, blue line), and S3 (wave run-up, red line).

955 **Figure 9.** Average maximum increase in salinity (in $\text{g TDS L}^{-1} \text{min}^{-1}$) and average total increase
956 in salinity during LSI (in g TDS L^{-1}), as observed in the ERT measurements between 14
957 November and 11 December 2014, grouped for LSI with sea-levels larger or equal to the
958 MHW, the MHW, and the MHWS.

959 **Figure 10.** Average increase in groundwater salinity (in $\text{g TDS L}^{-1} \text{min}^{-1}$) between 14 November
960 and 11 December 2014, as observed in the ERT measurements (gray), model scenario S1 (SWL,
961 blue), and model scenario S3 (wave run-up, red), grouped by the measured or simulated change
962 in groundwater head (in cm) at monitoring well D2 and sampled with a 30 minute interval.

963

964 **Figure 11.** Change in salinity (g TDS L^{-1}) with respect to the initial salinity distribution, for the
965 observed salinity (gray line), model scenario S1 (SWL, blue line), S2 (wave set-up, green line),
966 and S3 (wave run-up, red line). Instances of LSI [m] of (sections of) the transect are shown with
967 dark grey bars. The letters A, B and C mark the time of the three images shown in Figure 13.

968 **Figure 12.** Change in salinity (g TDS L^{-1}) with respect to the initial salinity distribution, for the
969 observed salinity (gray line), and model scenario S3 (wave run-up) with recharge (red line) and
970 without recharge (orange line). The precipitation is given in mm d^{-1} with black bars. The letters
971 A, B and C mark the time of the three images shown in Figure 13.

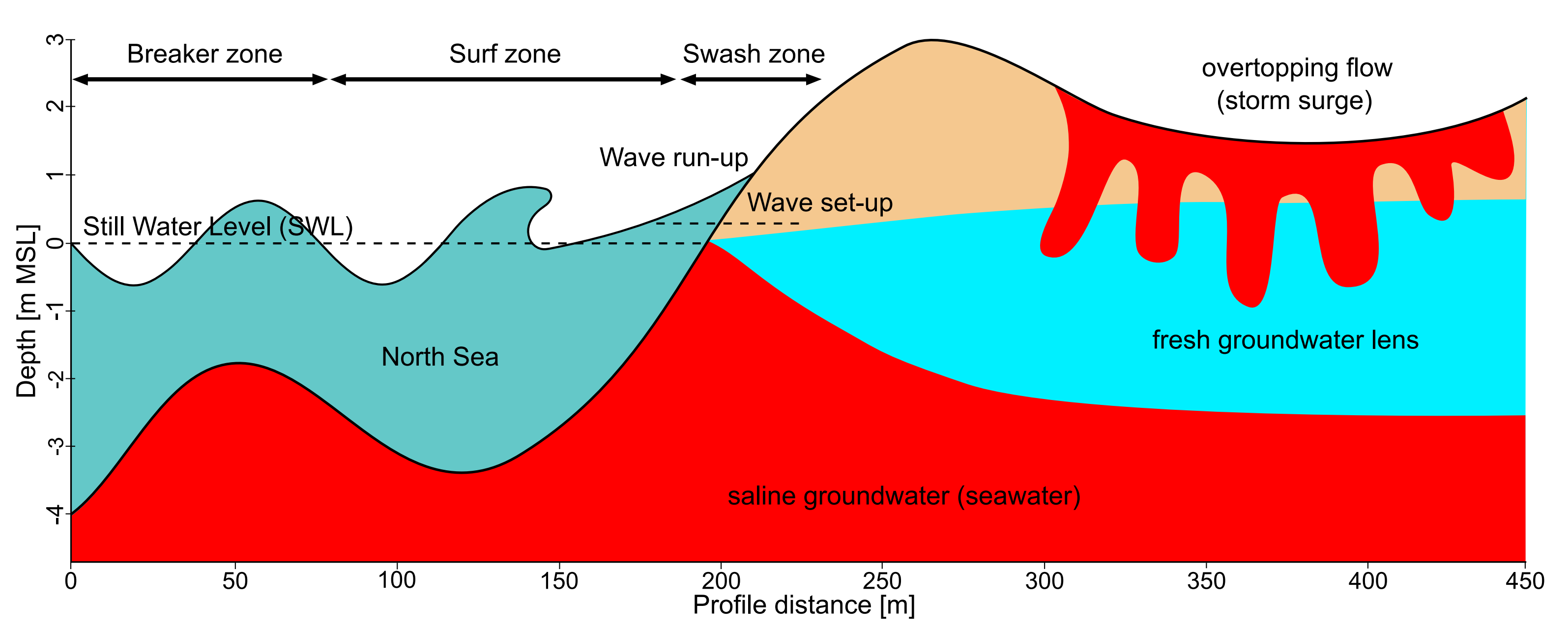
972 **Figure 13.** 2-D images of the measured (left) and the simulated groundwater salinity (right: S3,
973 wave run-up) for three instances: 14 November 11:00 (start of measurements); 1 December
974 15:00 (after a calm weather period); and 11 December 19:30 (after substantial inundations).
975 These instances are also indicated in Figure 11 and Figure 12 with letters A, B and C.

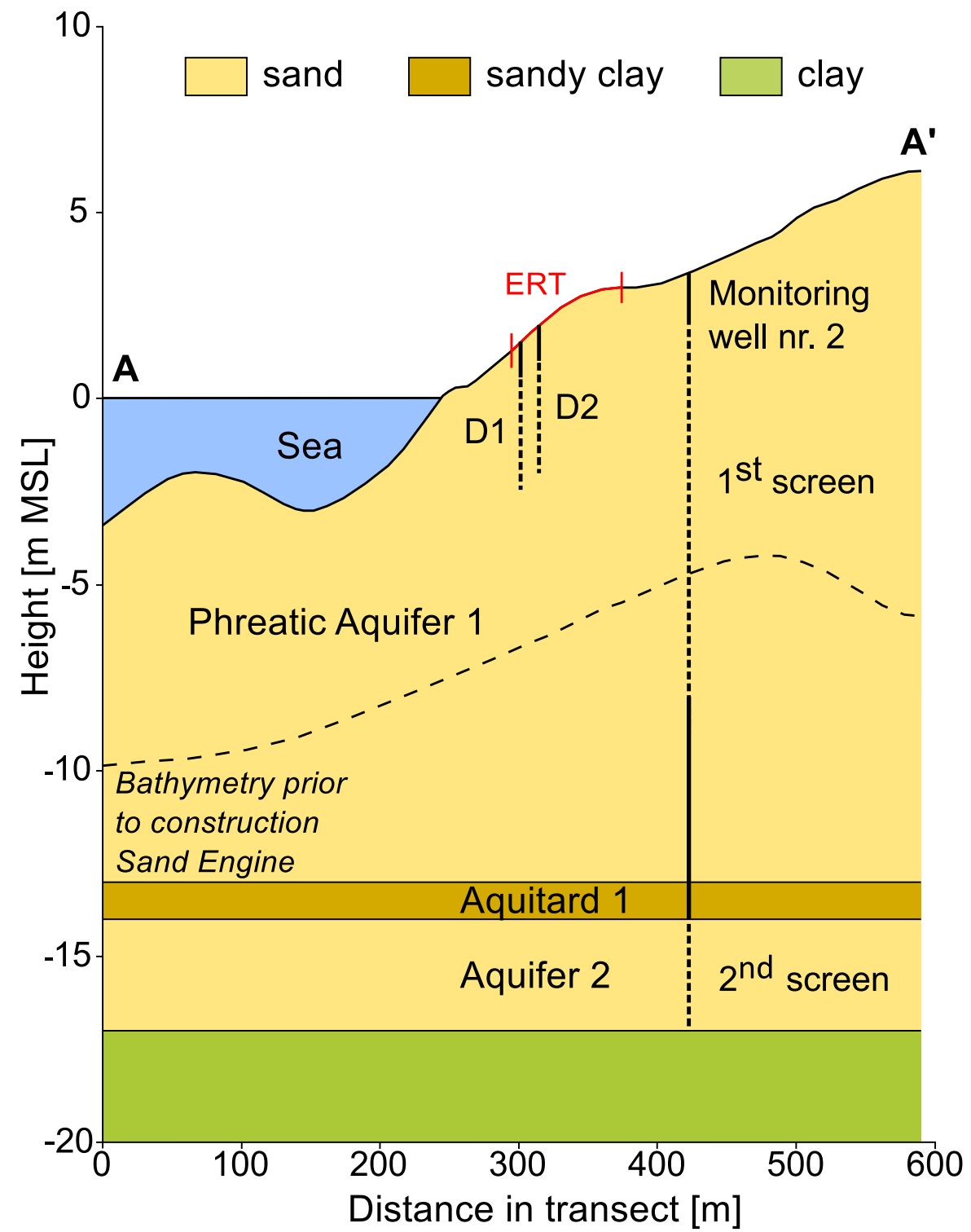
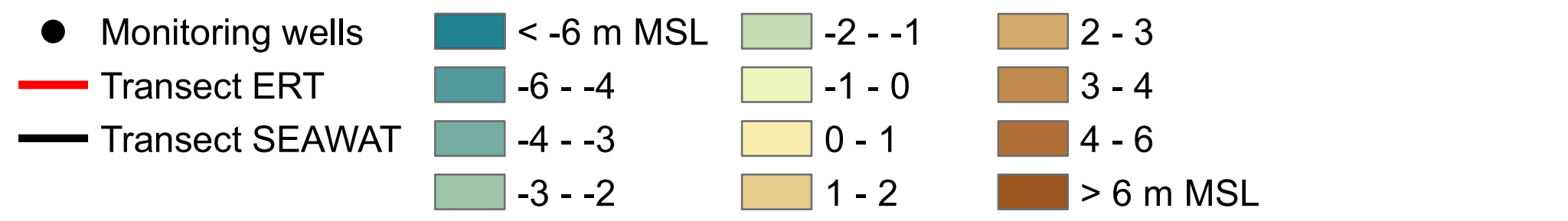
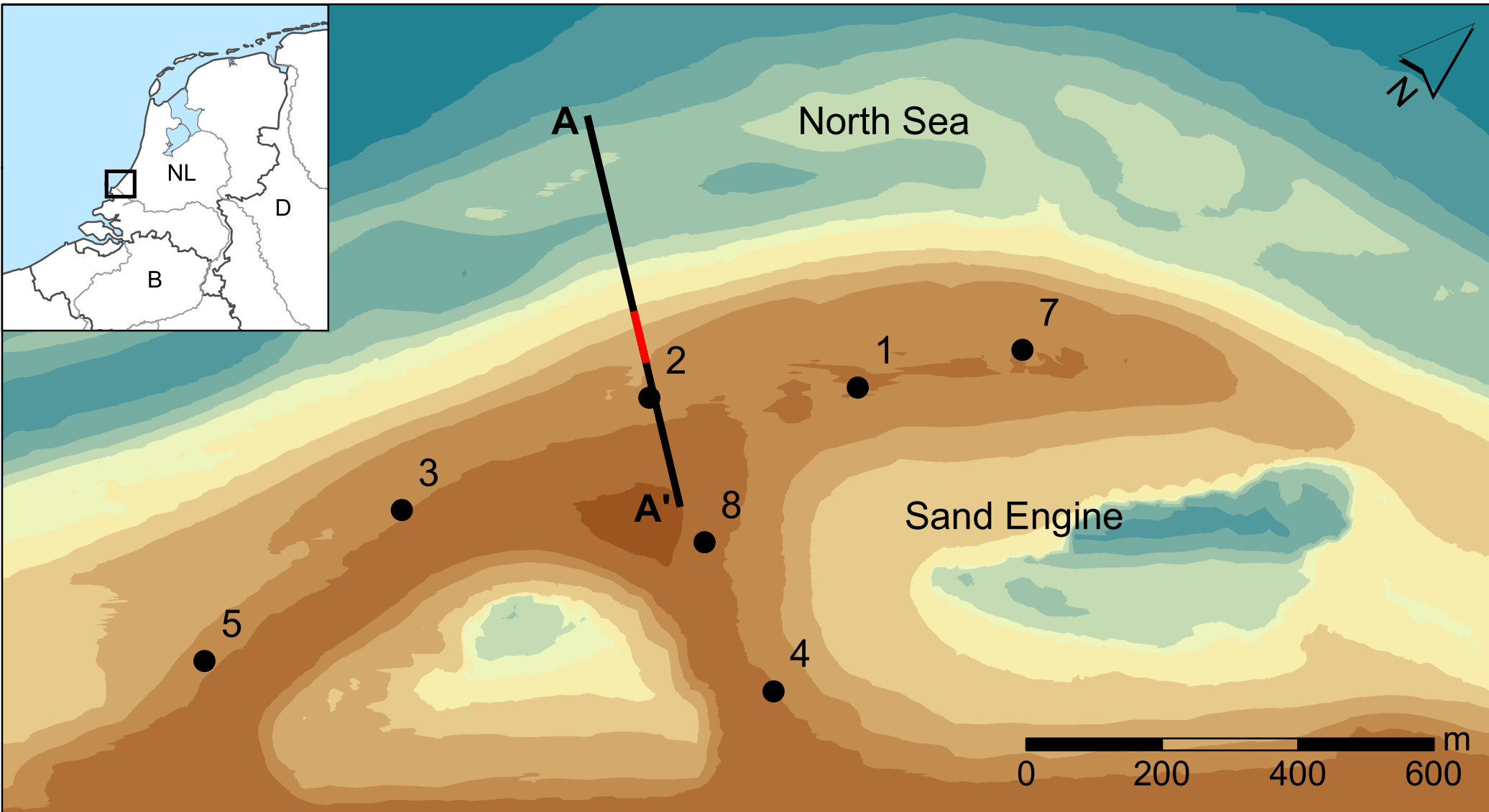
976 **Figure A1.** Simulated groundwater salinity of case 1 and 2

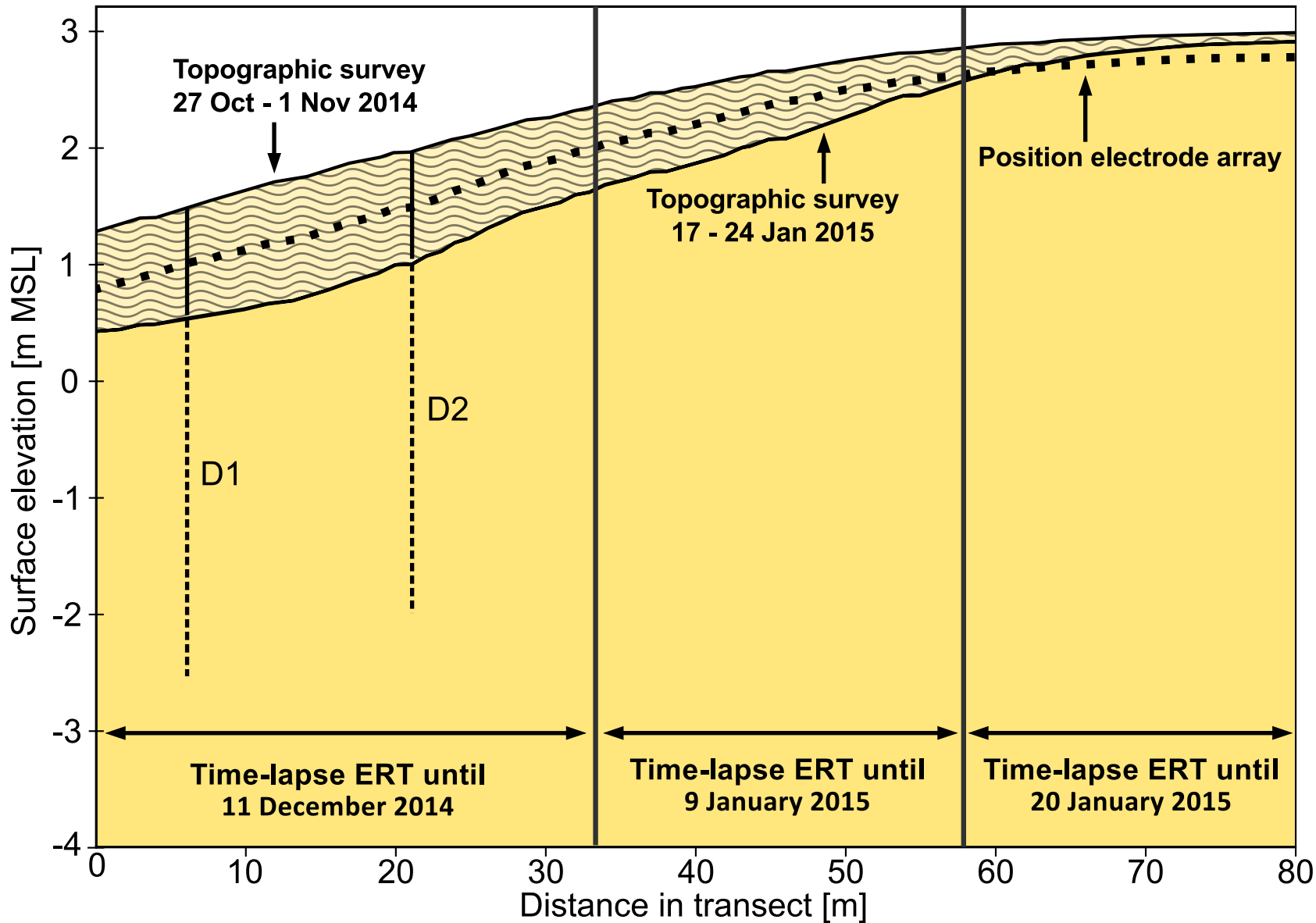
977 **Figure A2.** Inverted groundwater salinity of case 1 ‘MHW’, with L1 (top) or L2 (bottom)
978 minimization norms and an automatic (left) or constant (right) Lagrangian multiplier

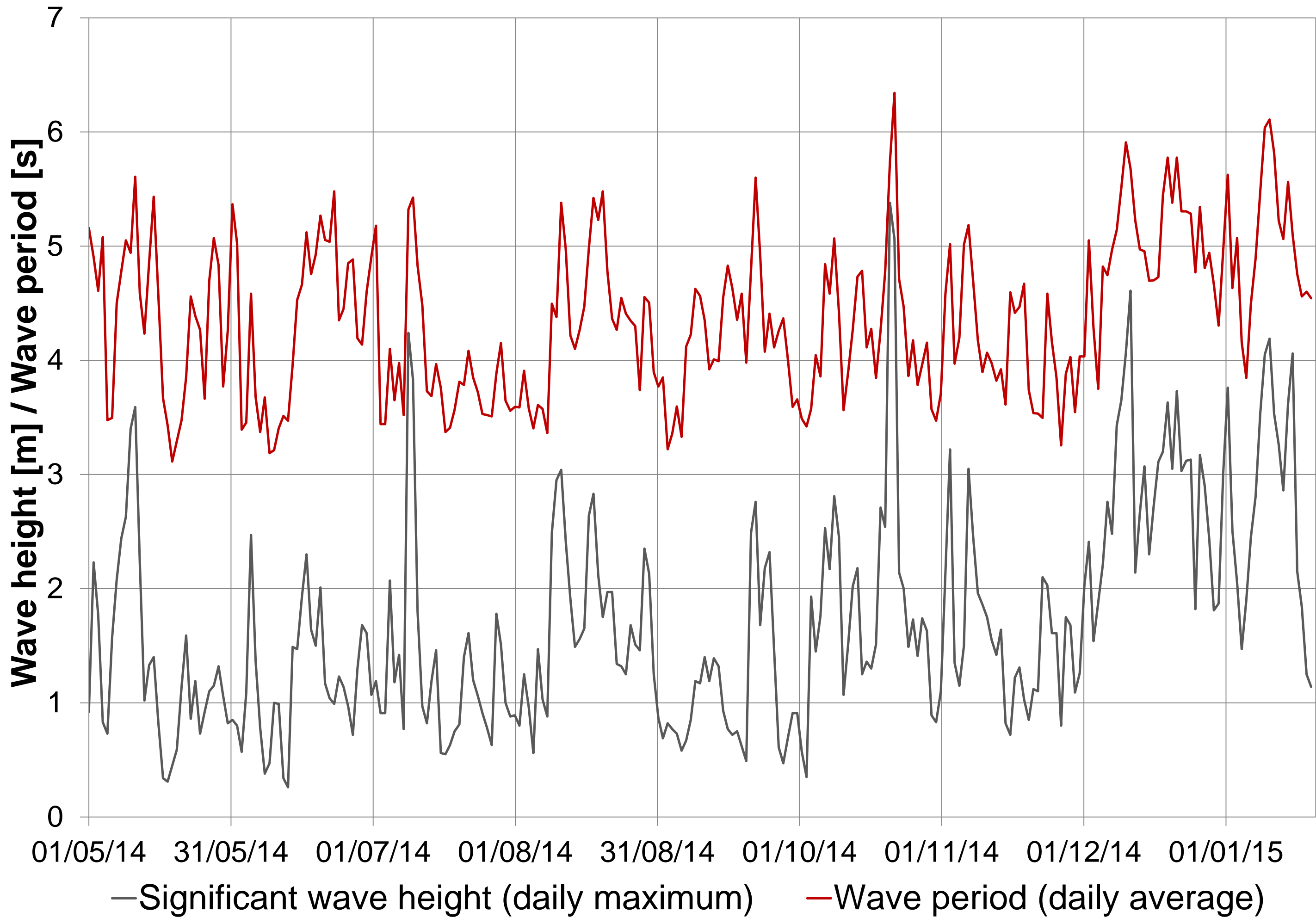
979 **Figure A3.** Inverted groundwater salinity of case 2 ‘LSI’, with L1 (top) or L2 (bottom)
980 minimization norms and an automatic (left) or constant (right) Lagrangian multiplier

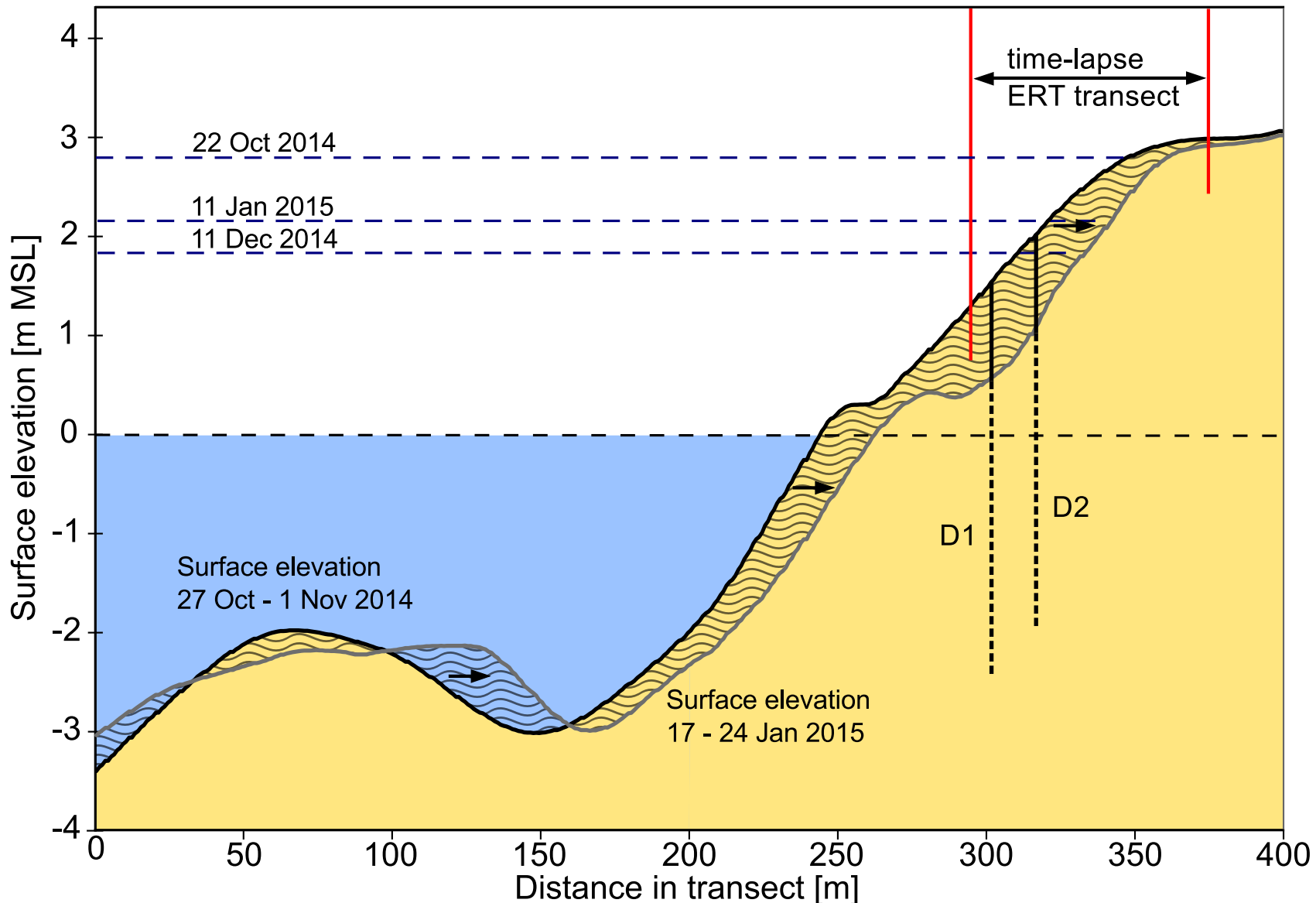
981

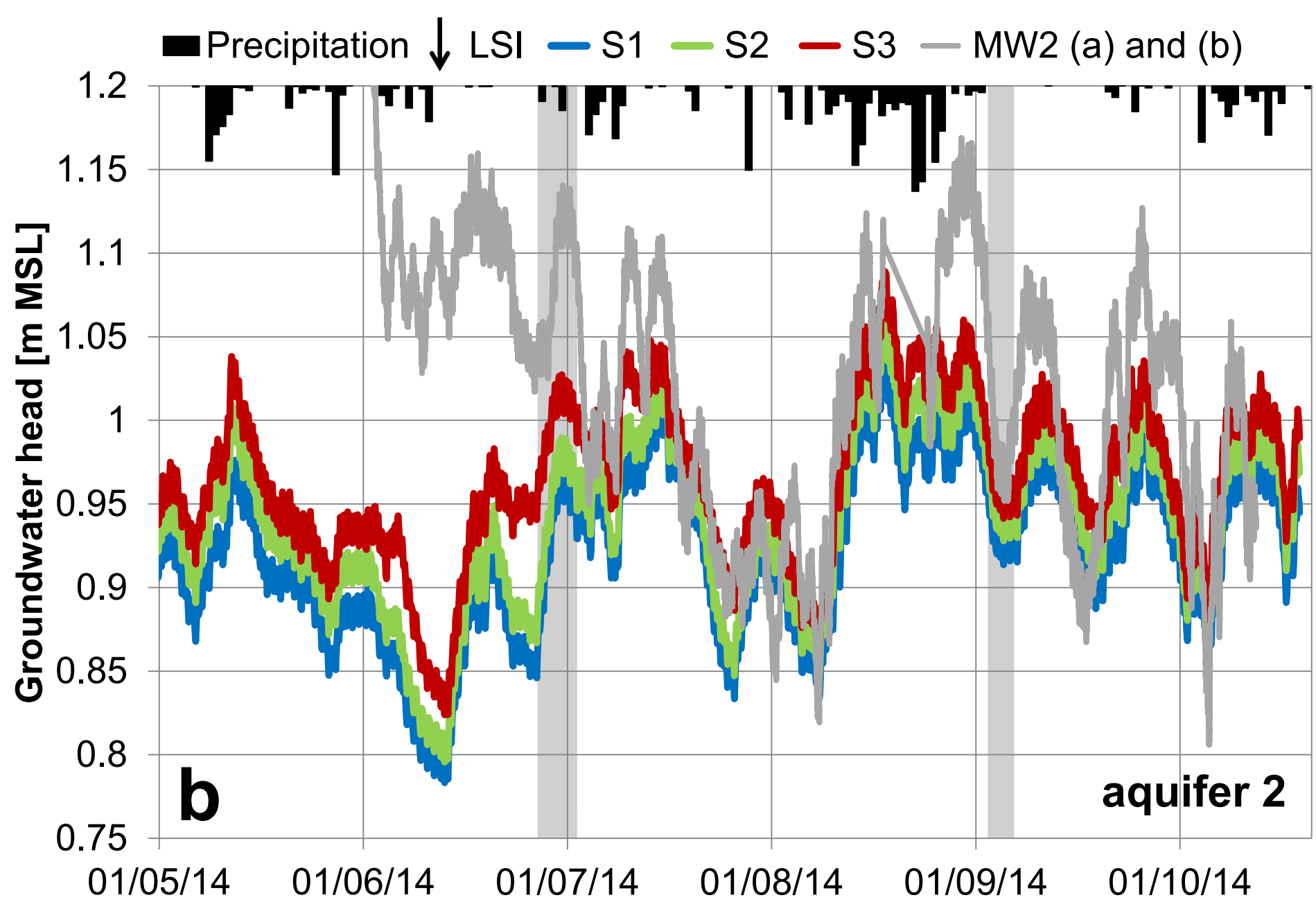
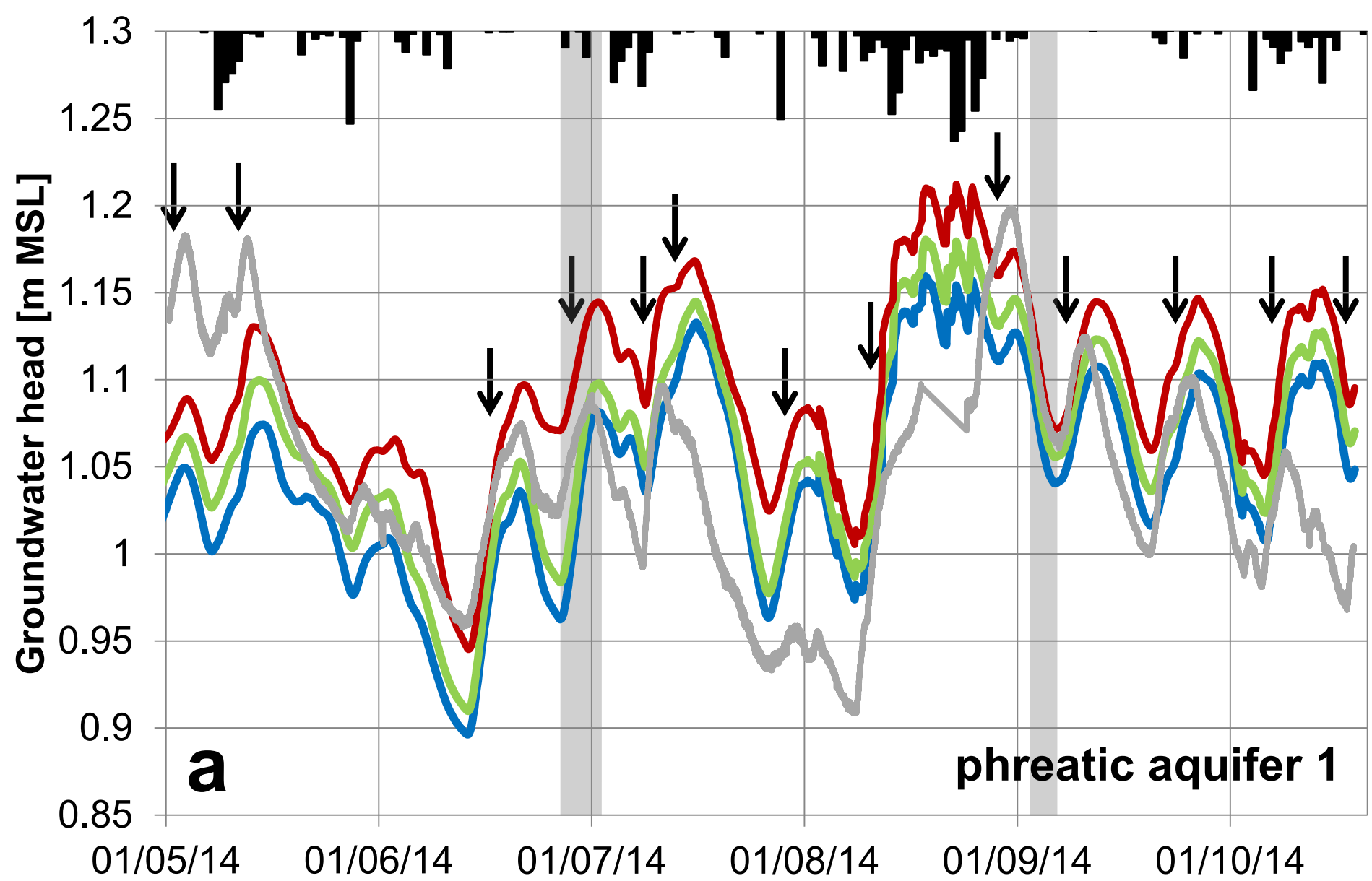


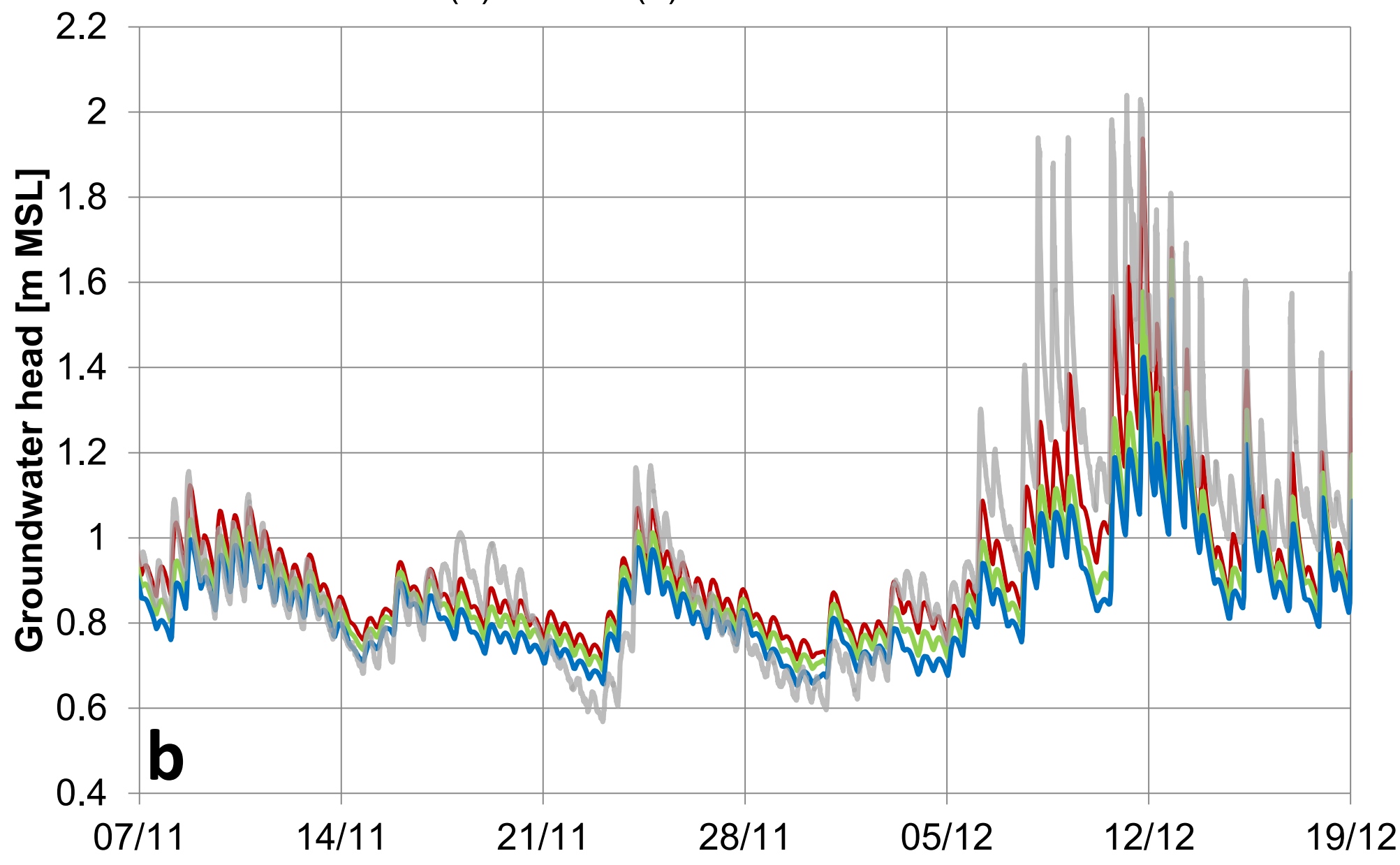
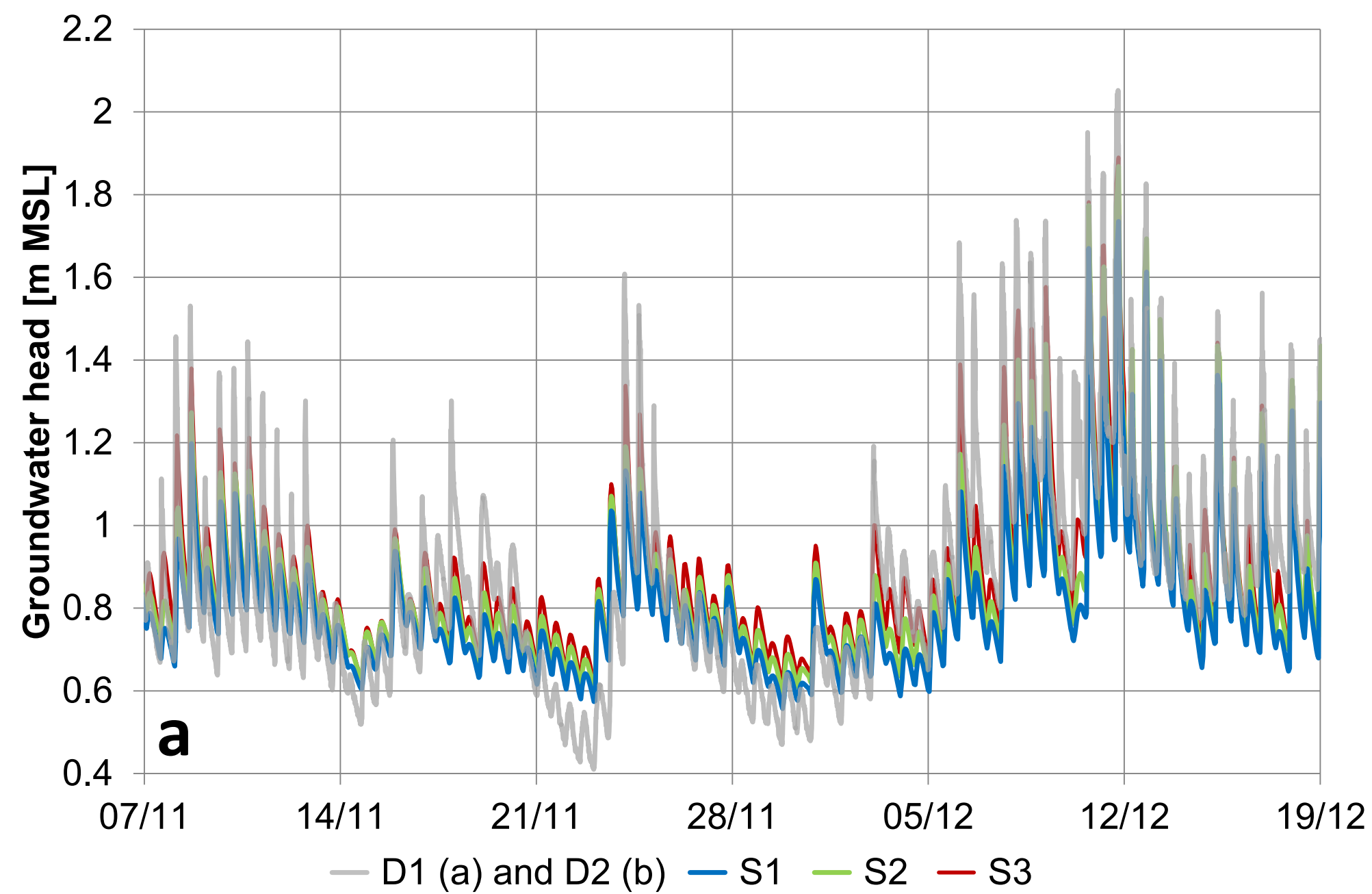


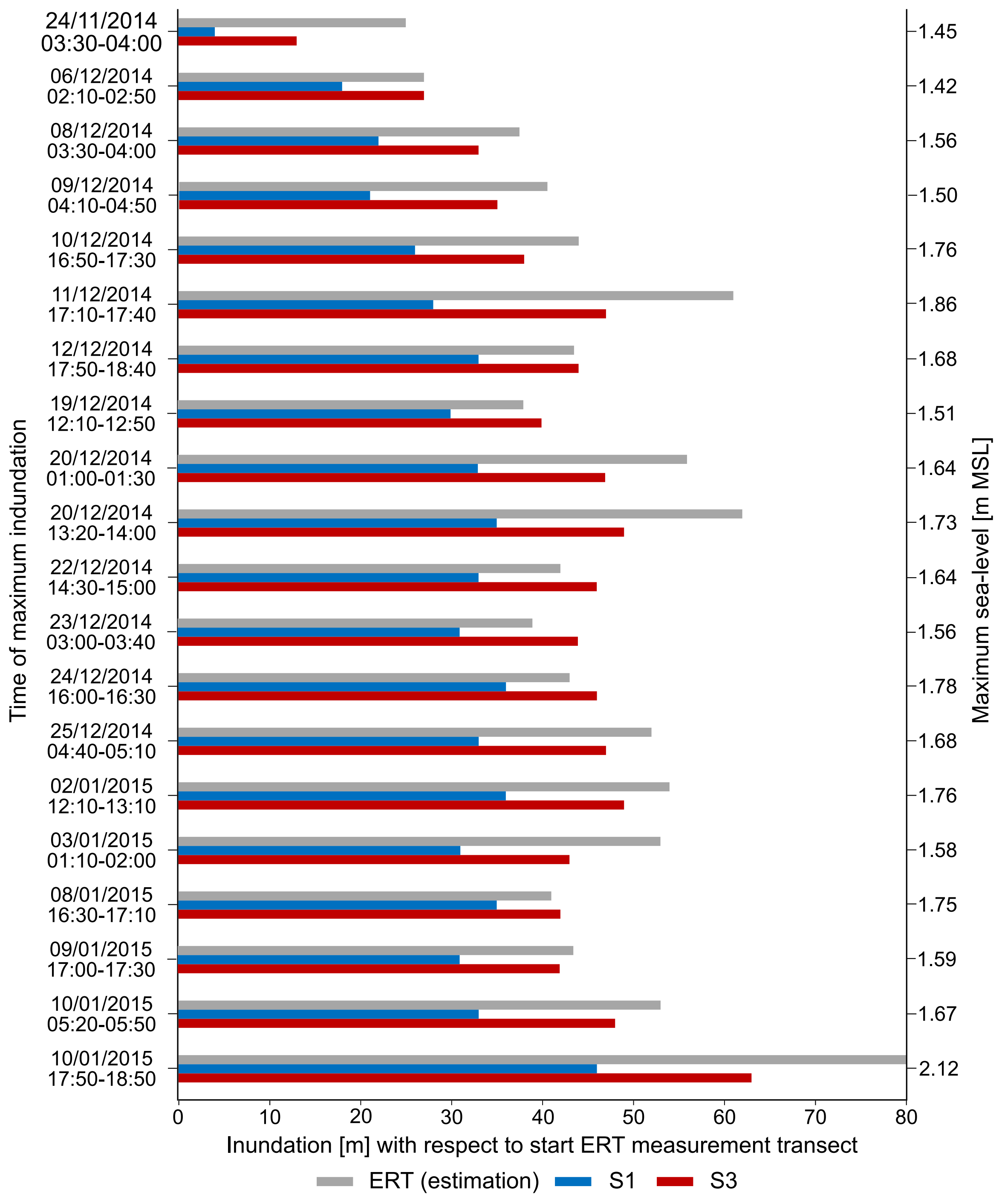


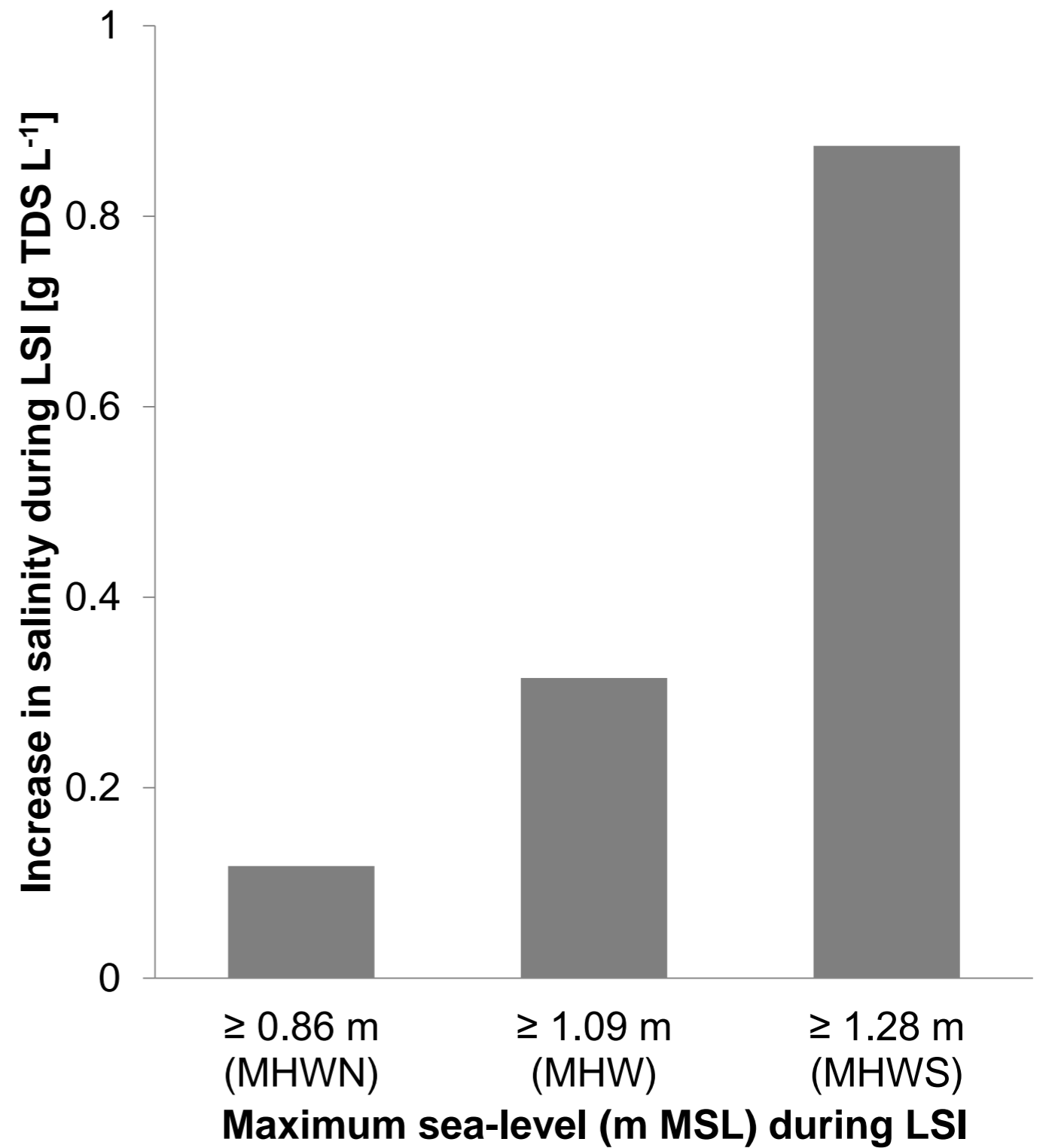
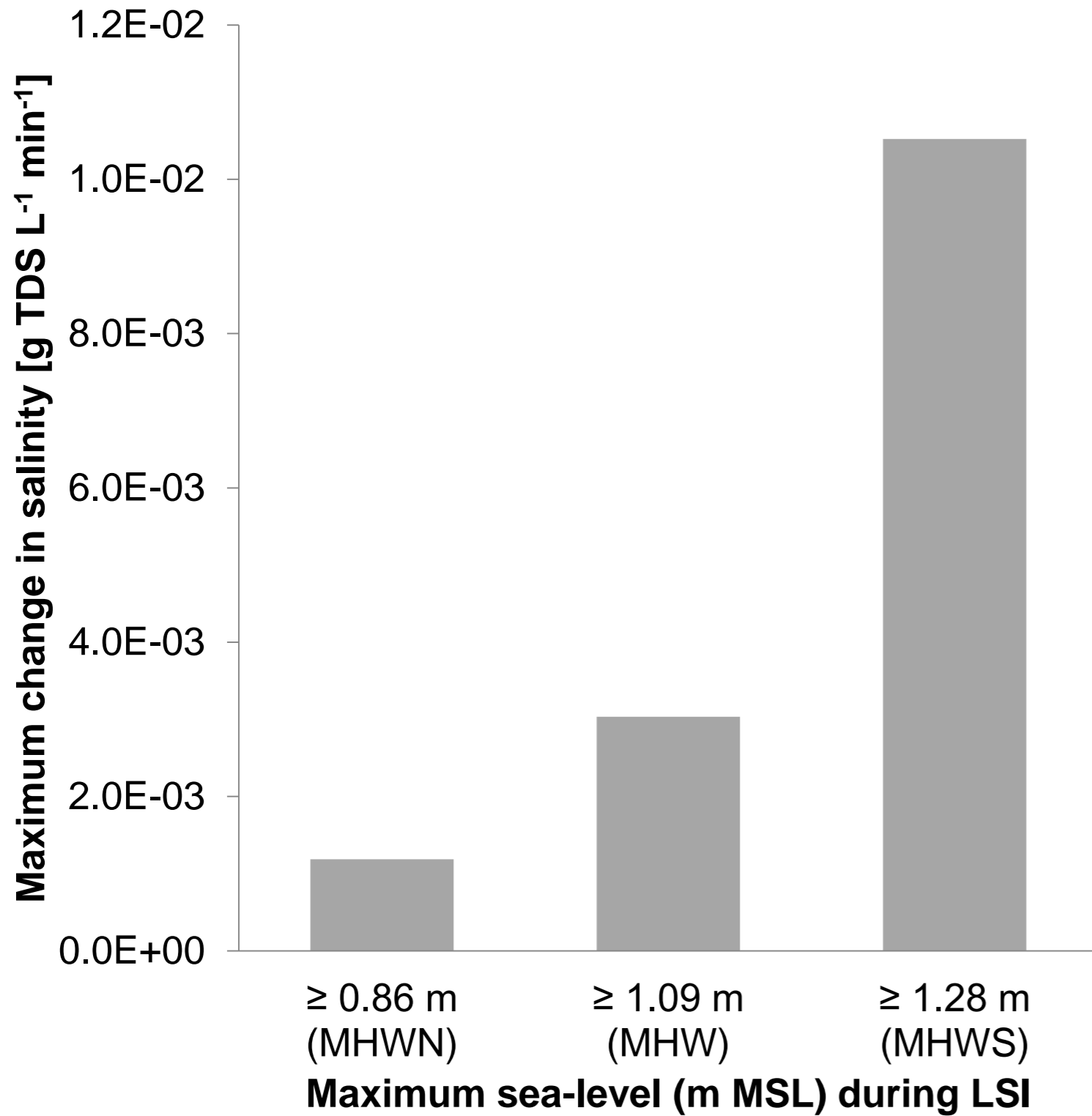


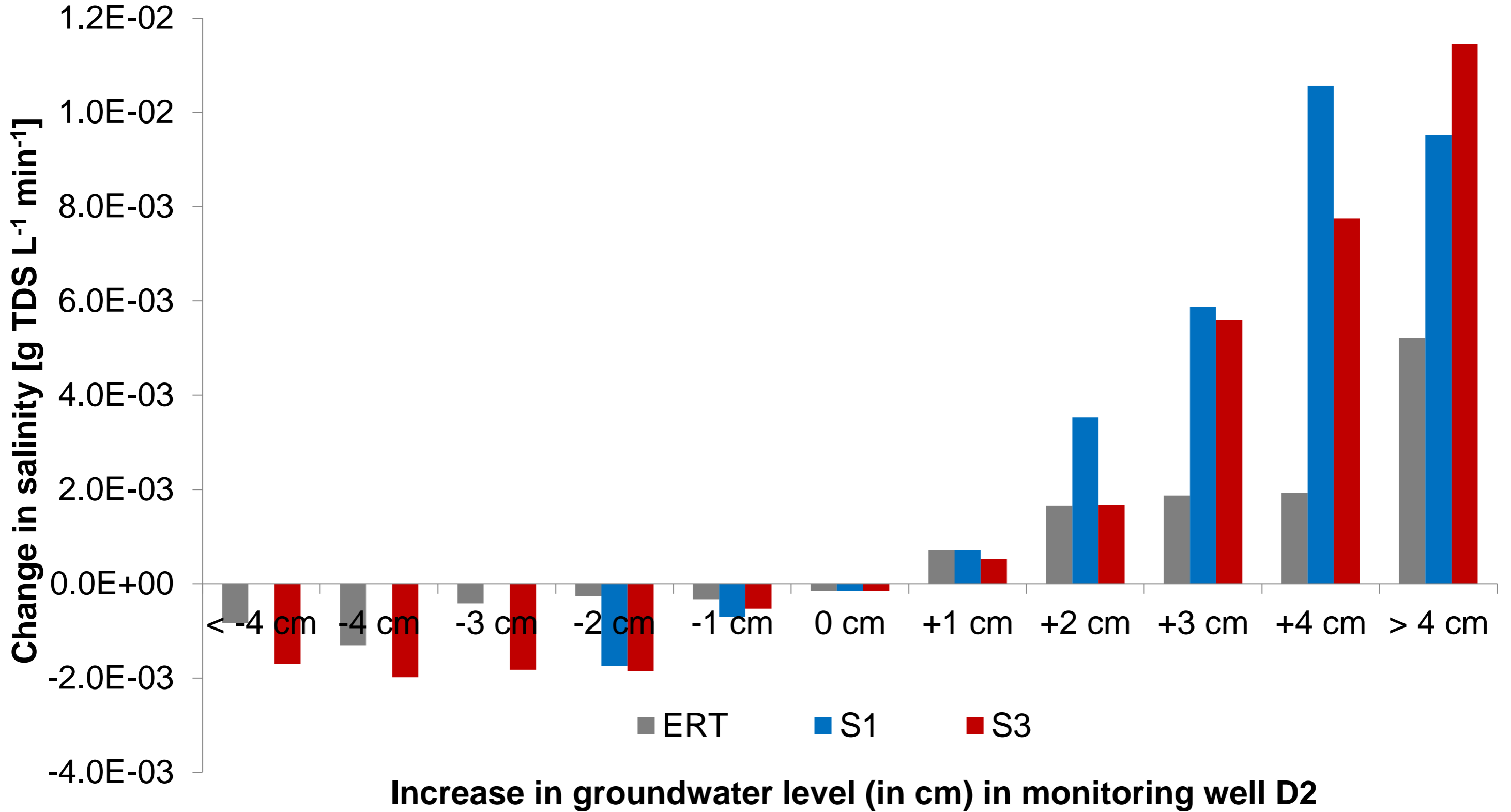


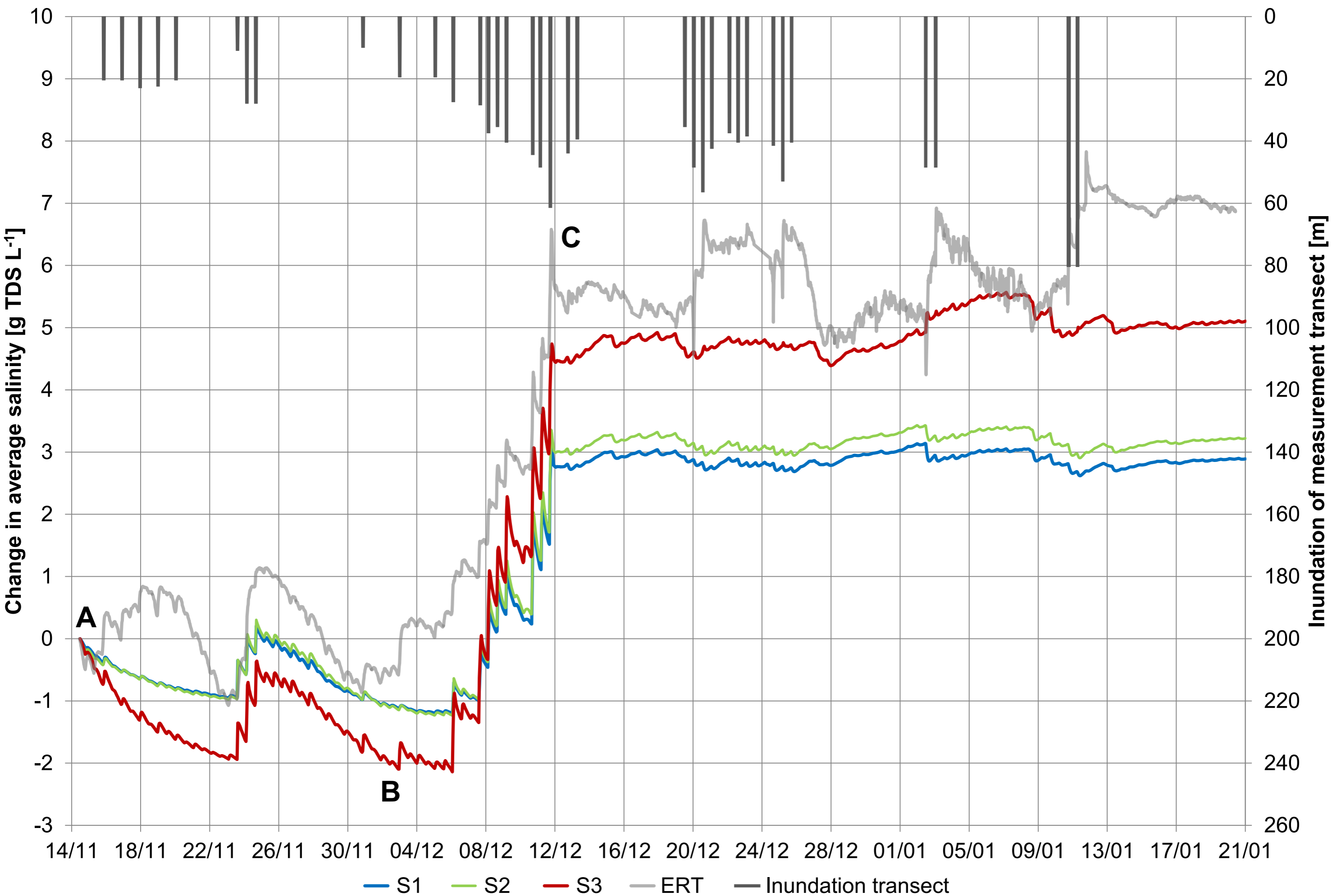


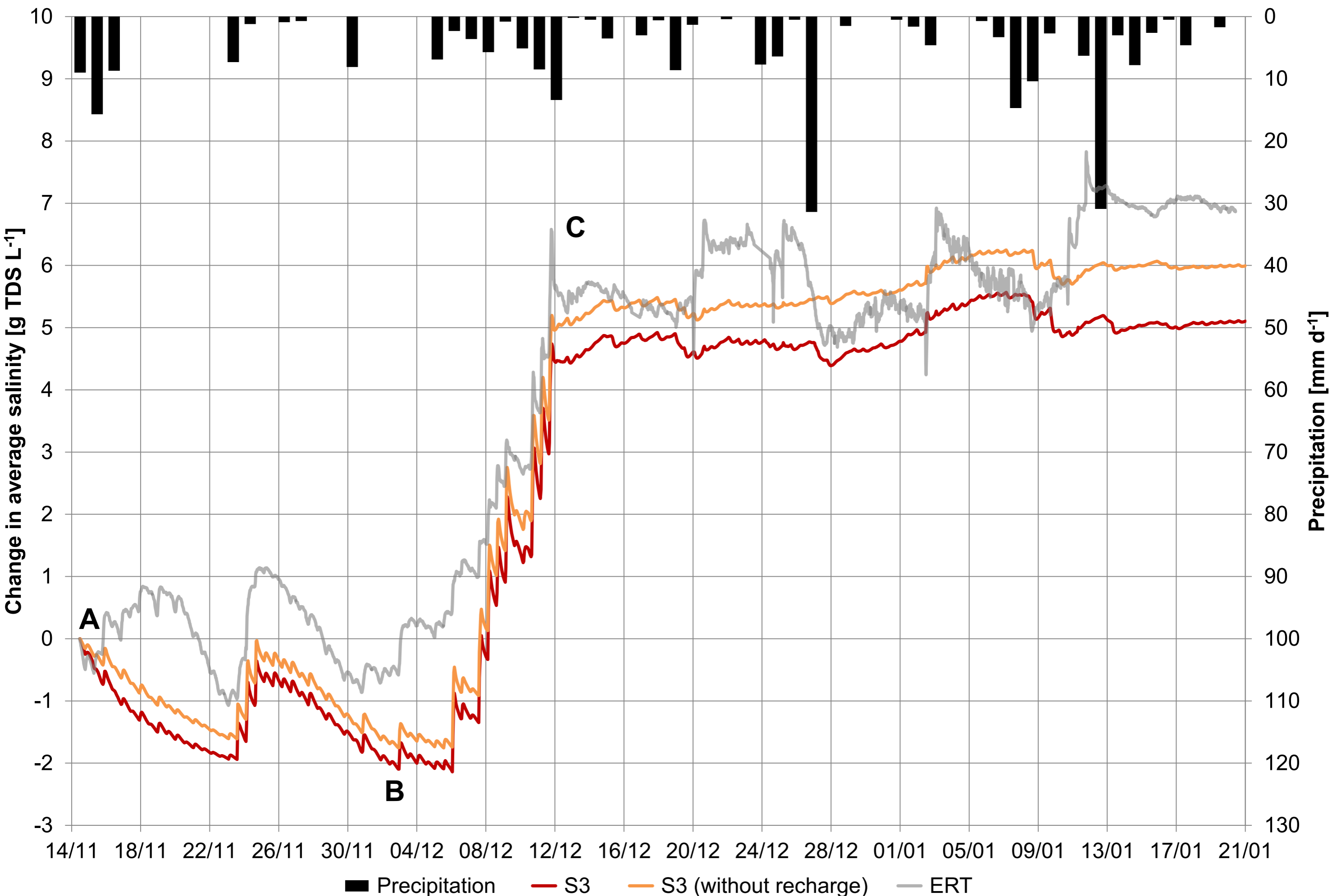


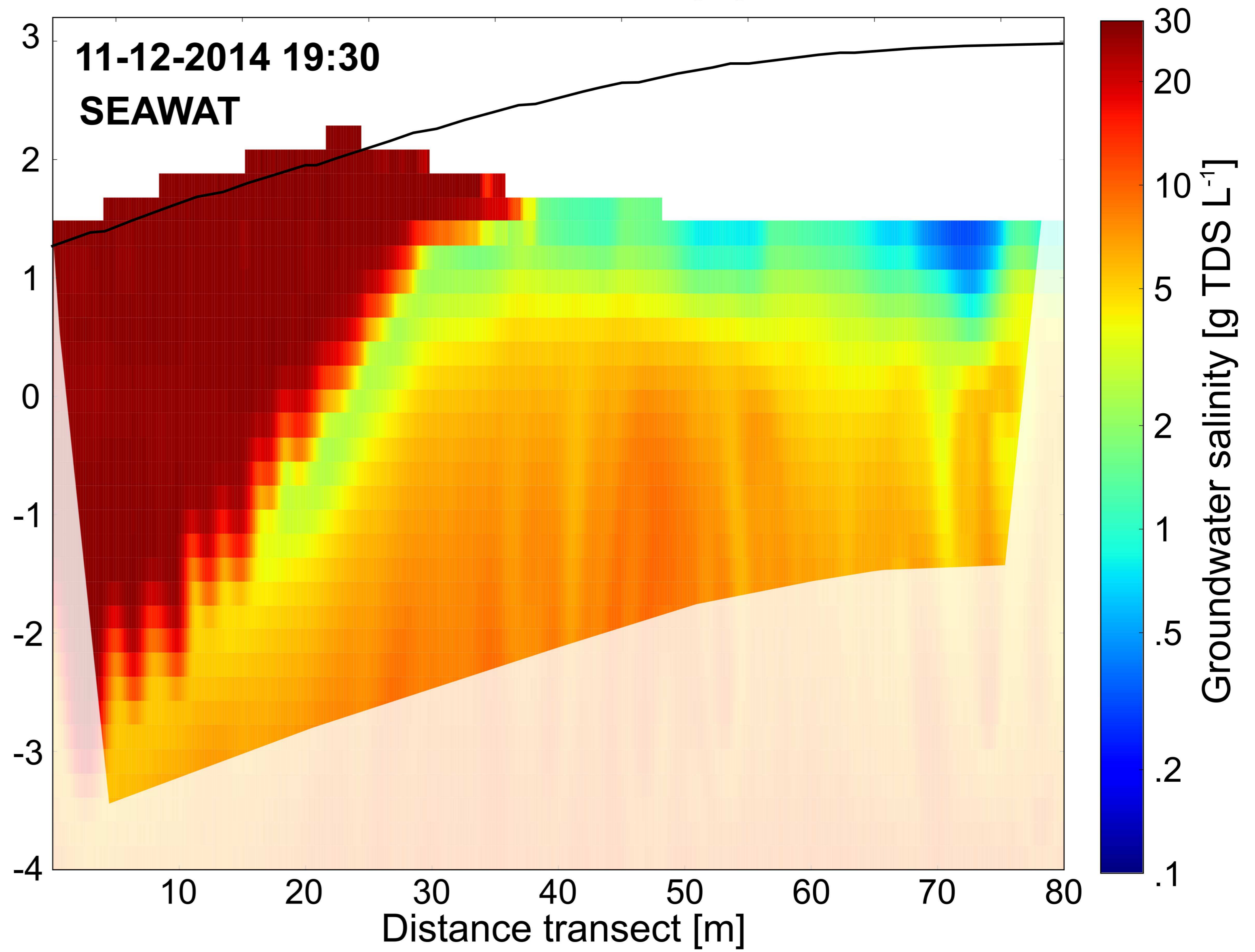
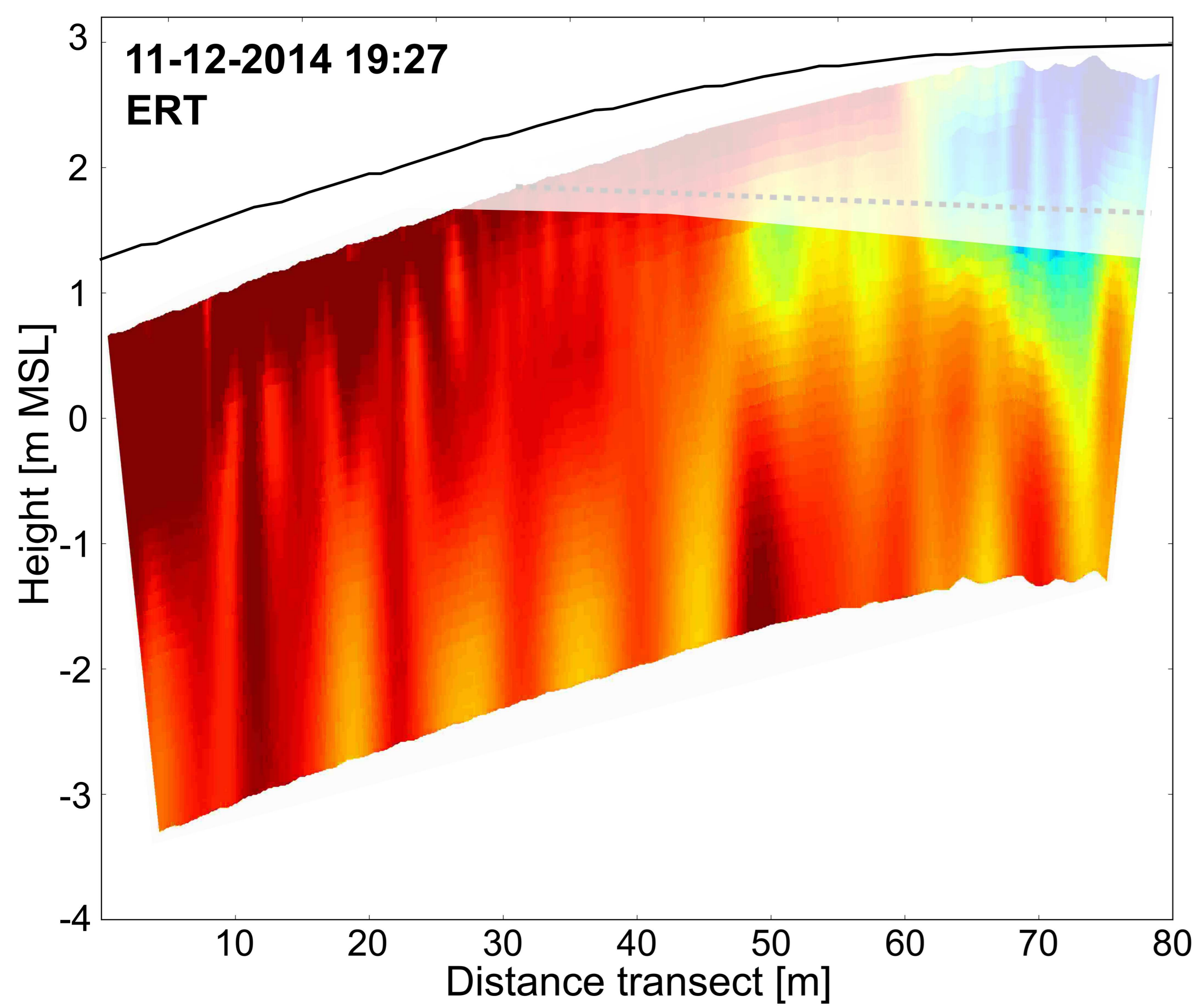
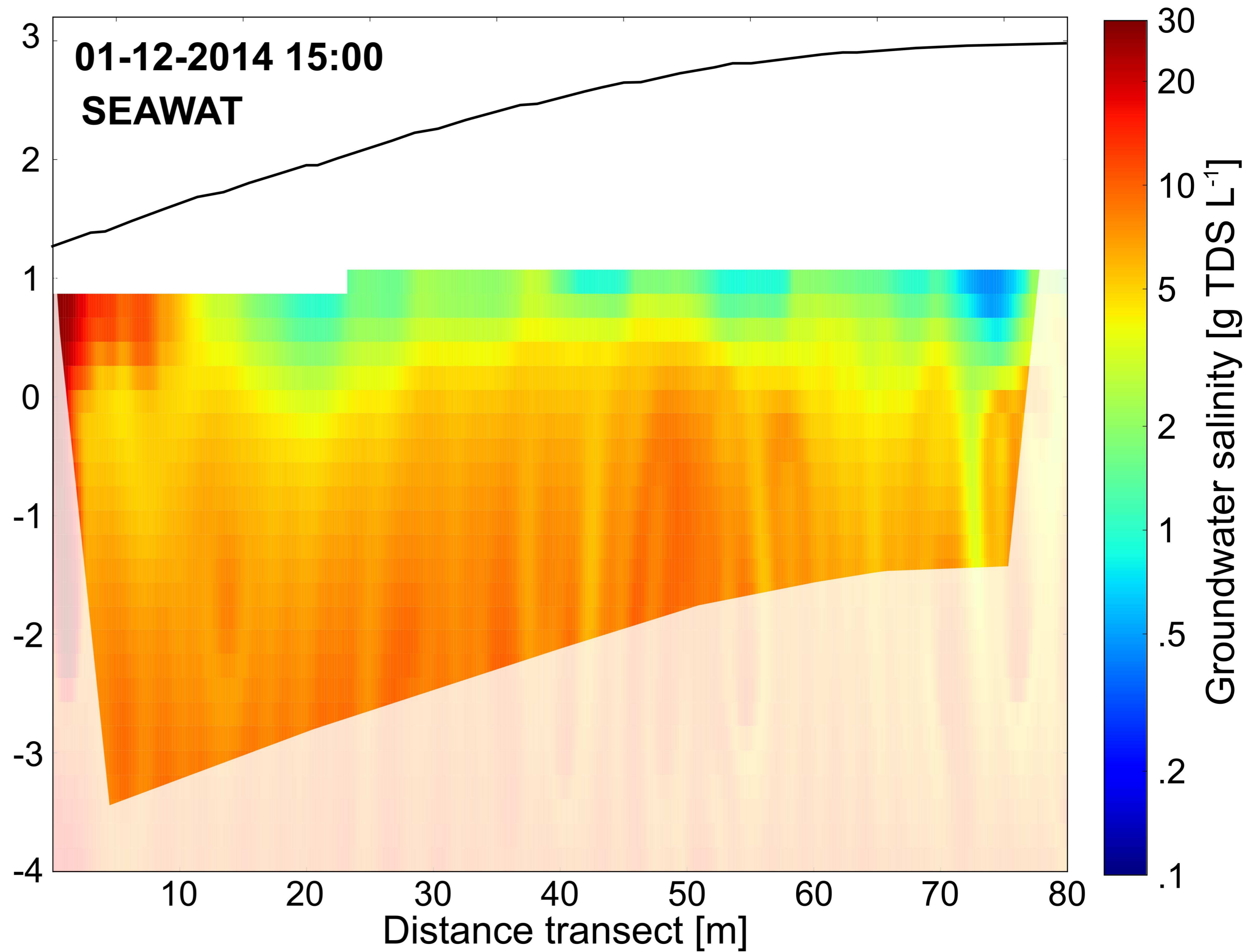
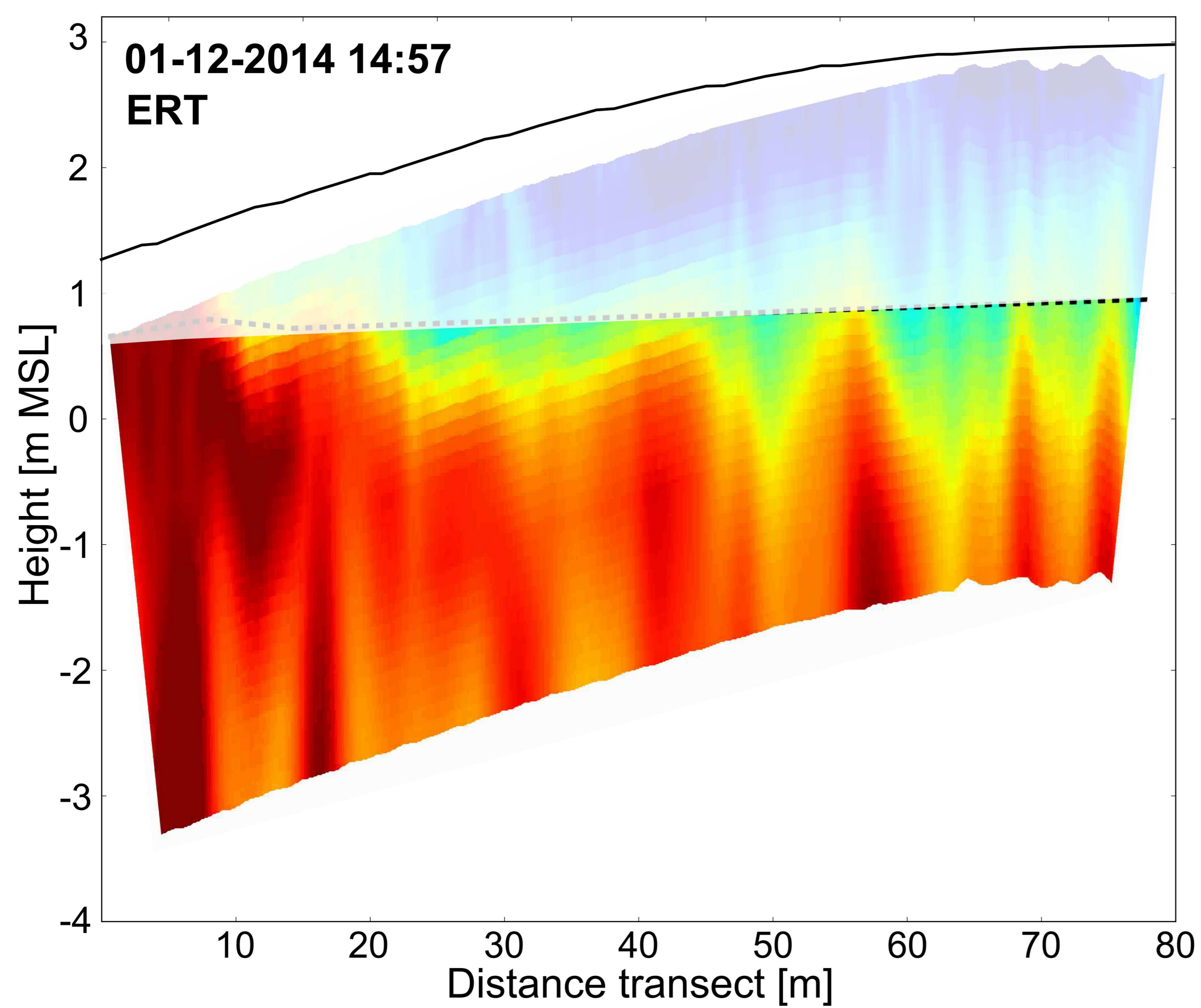
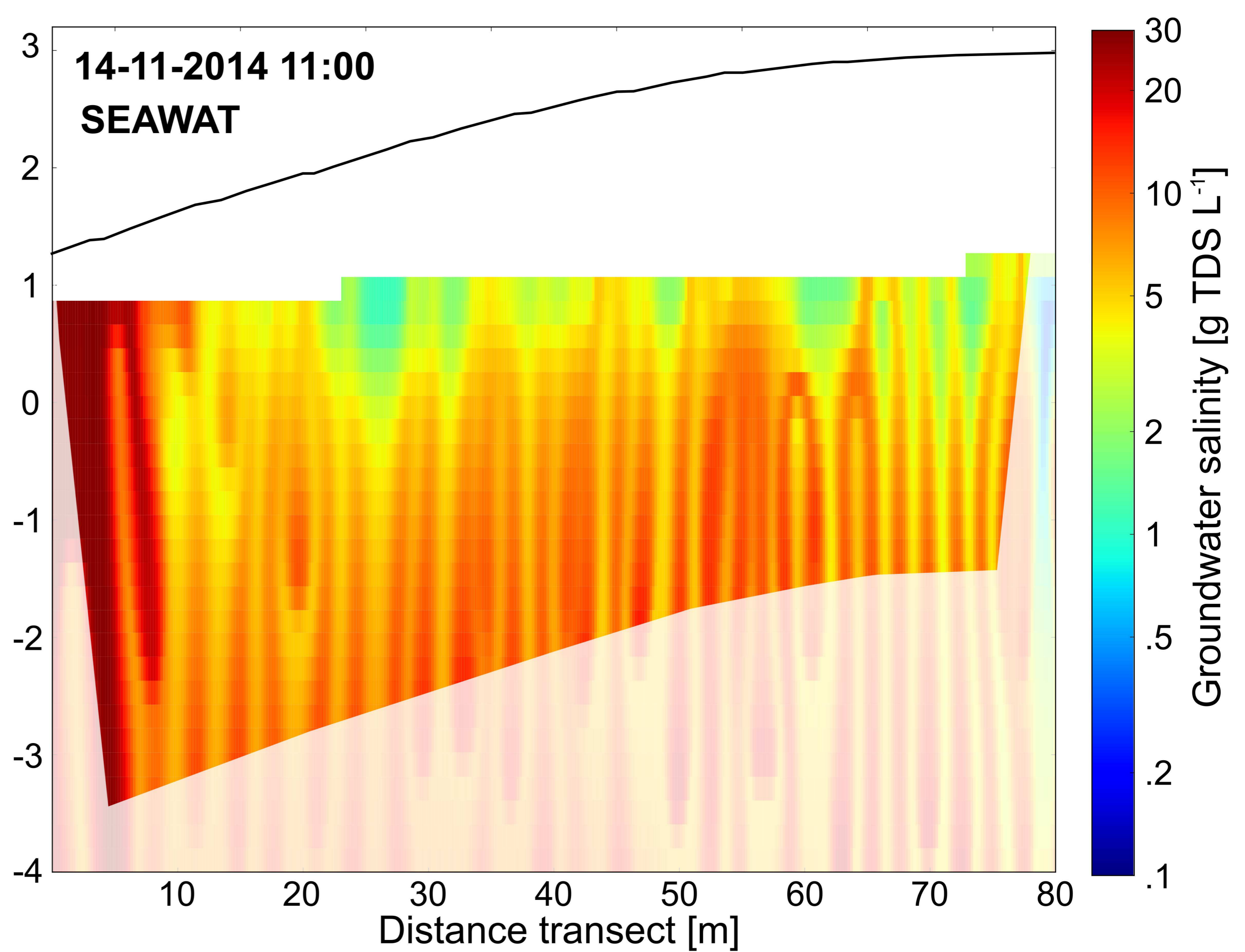
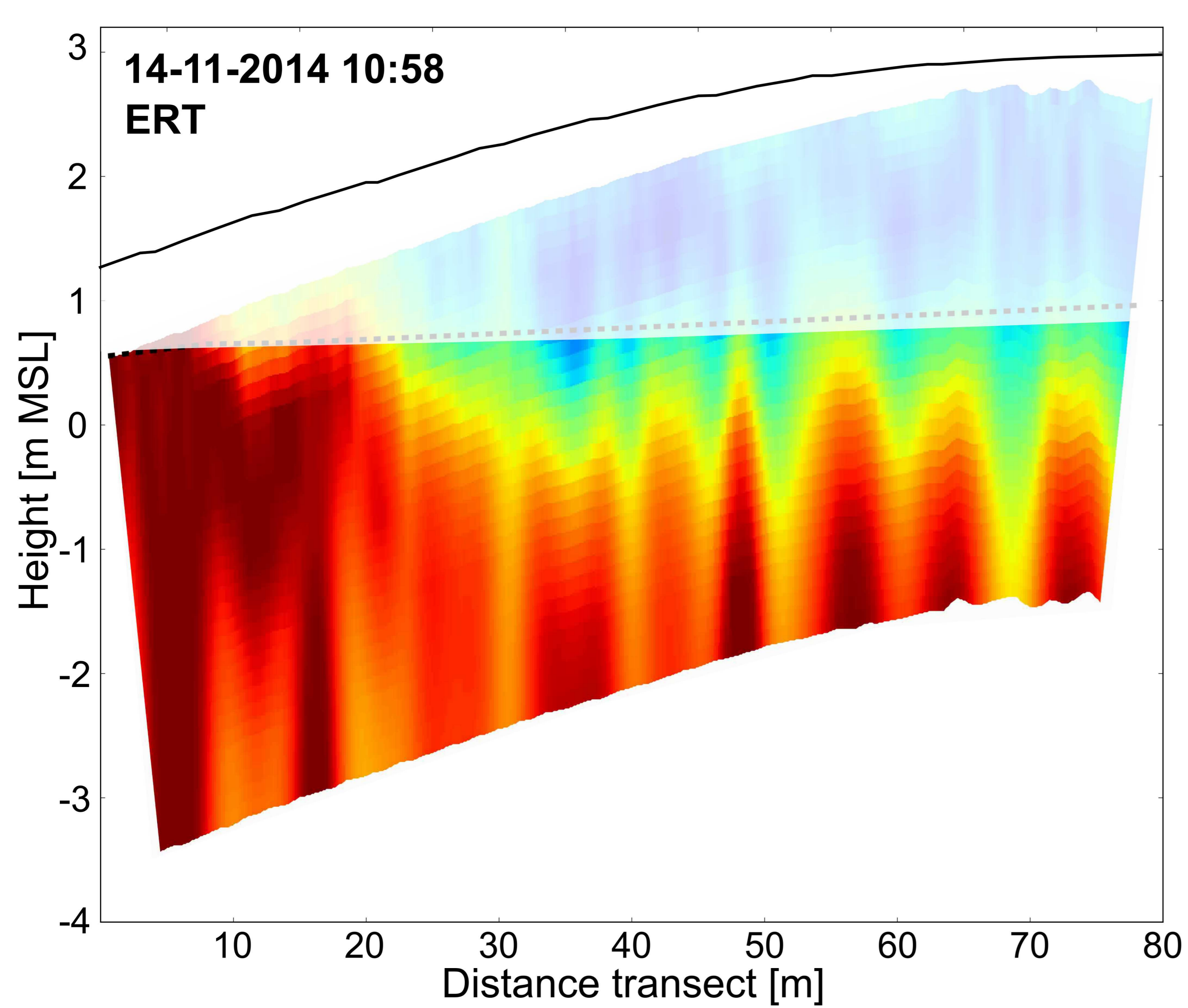


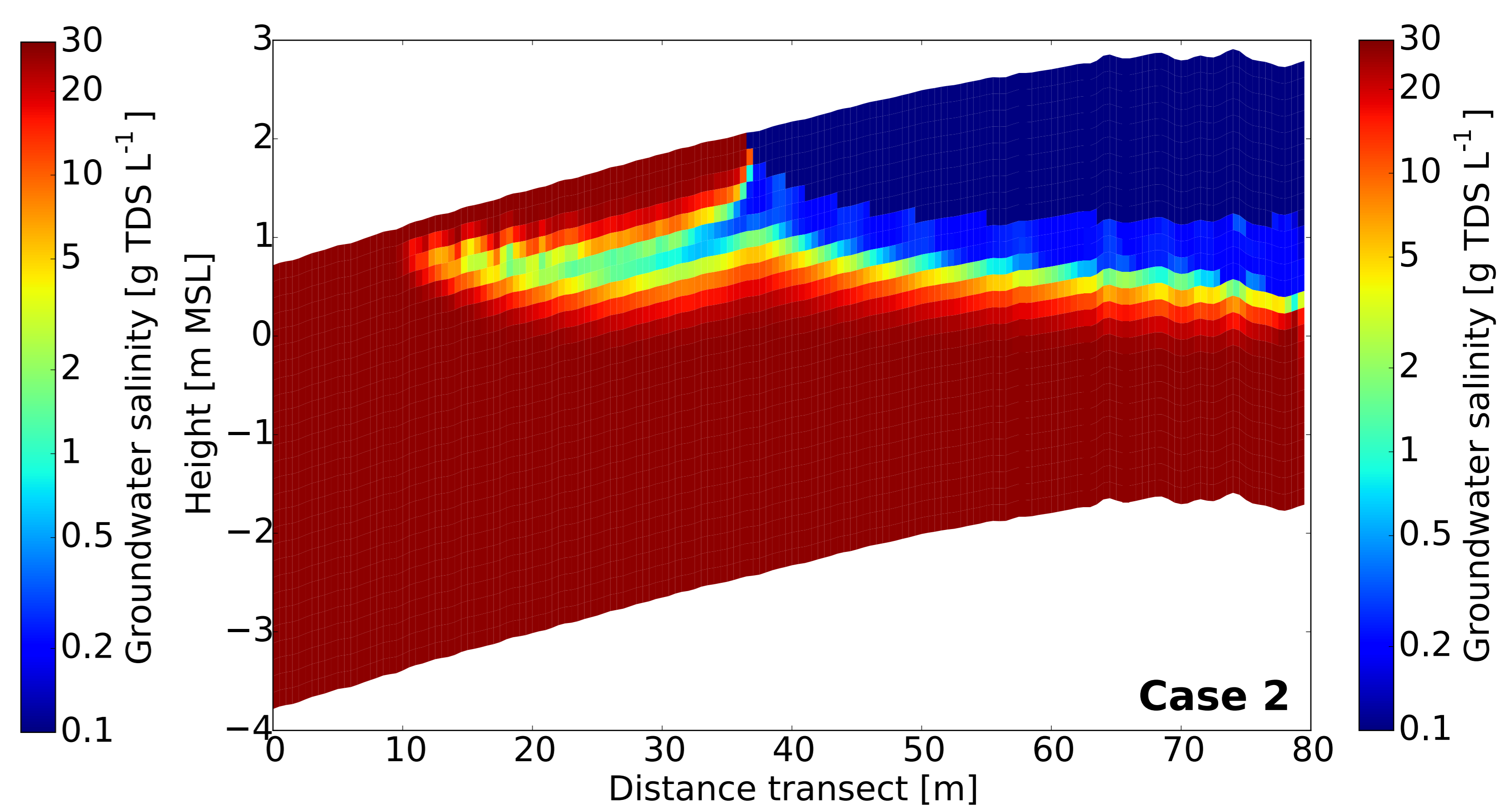
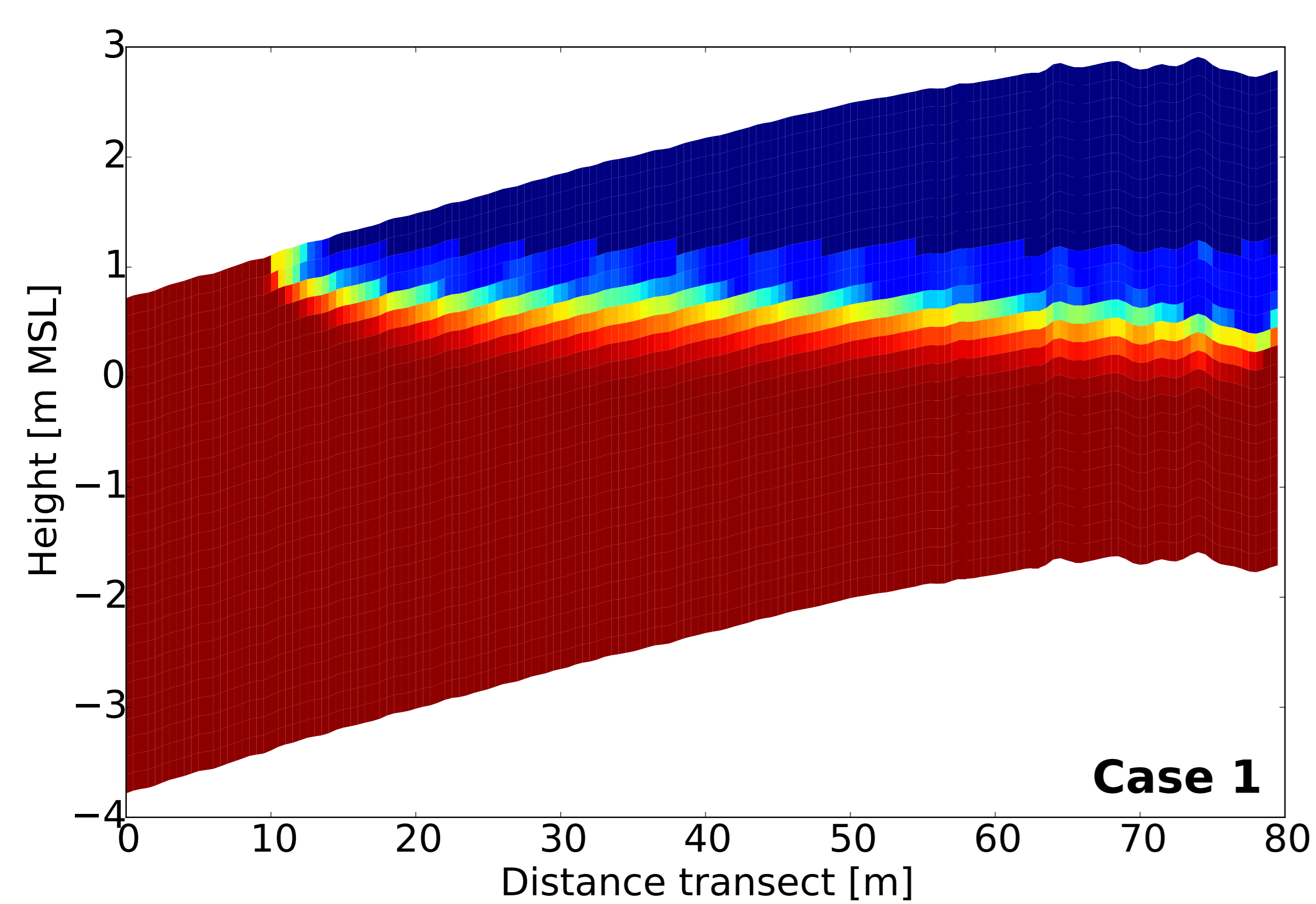




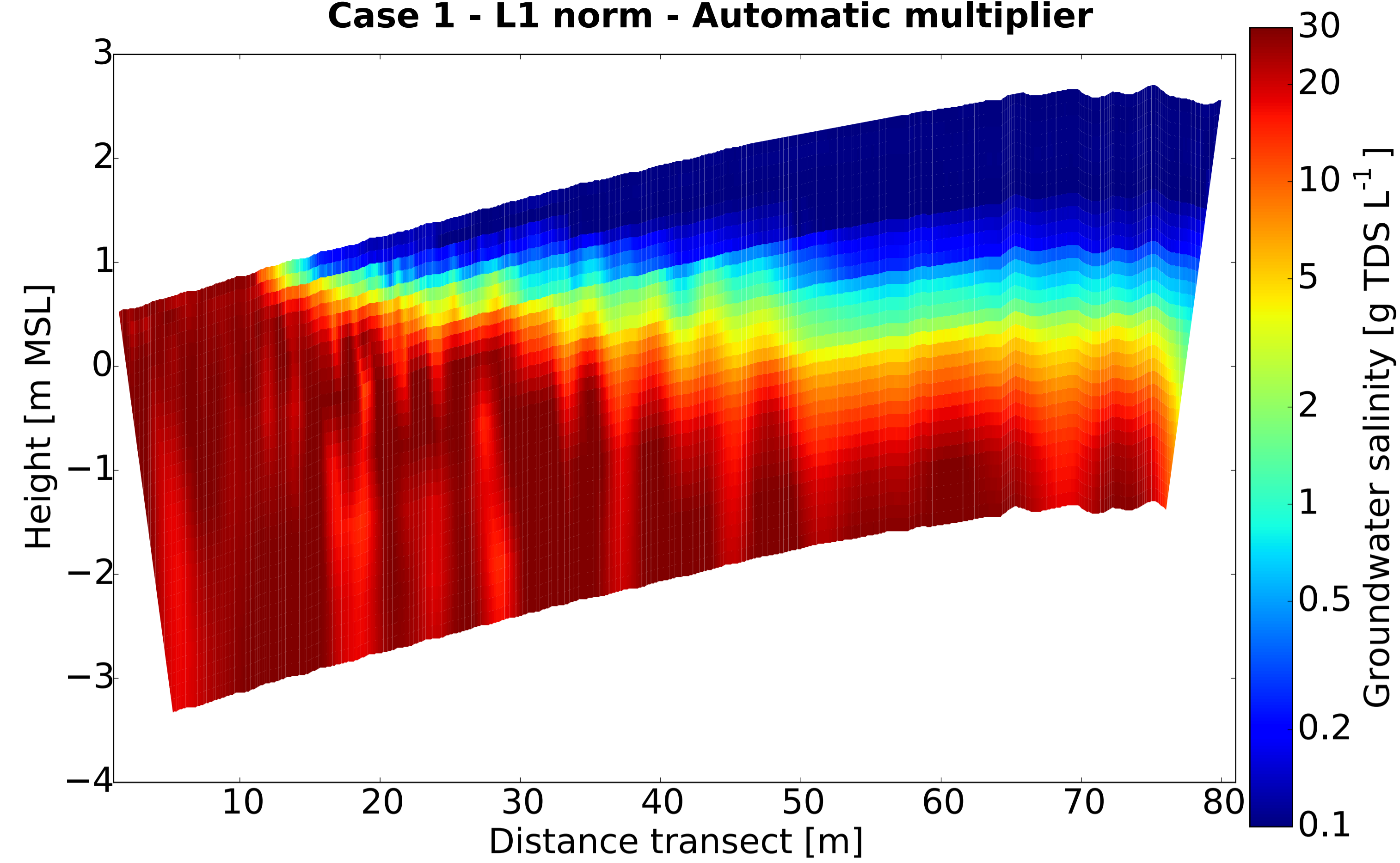




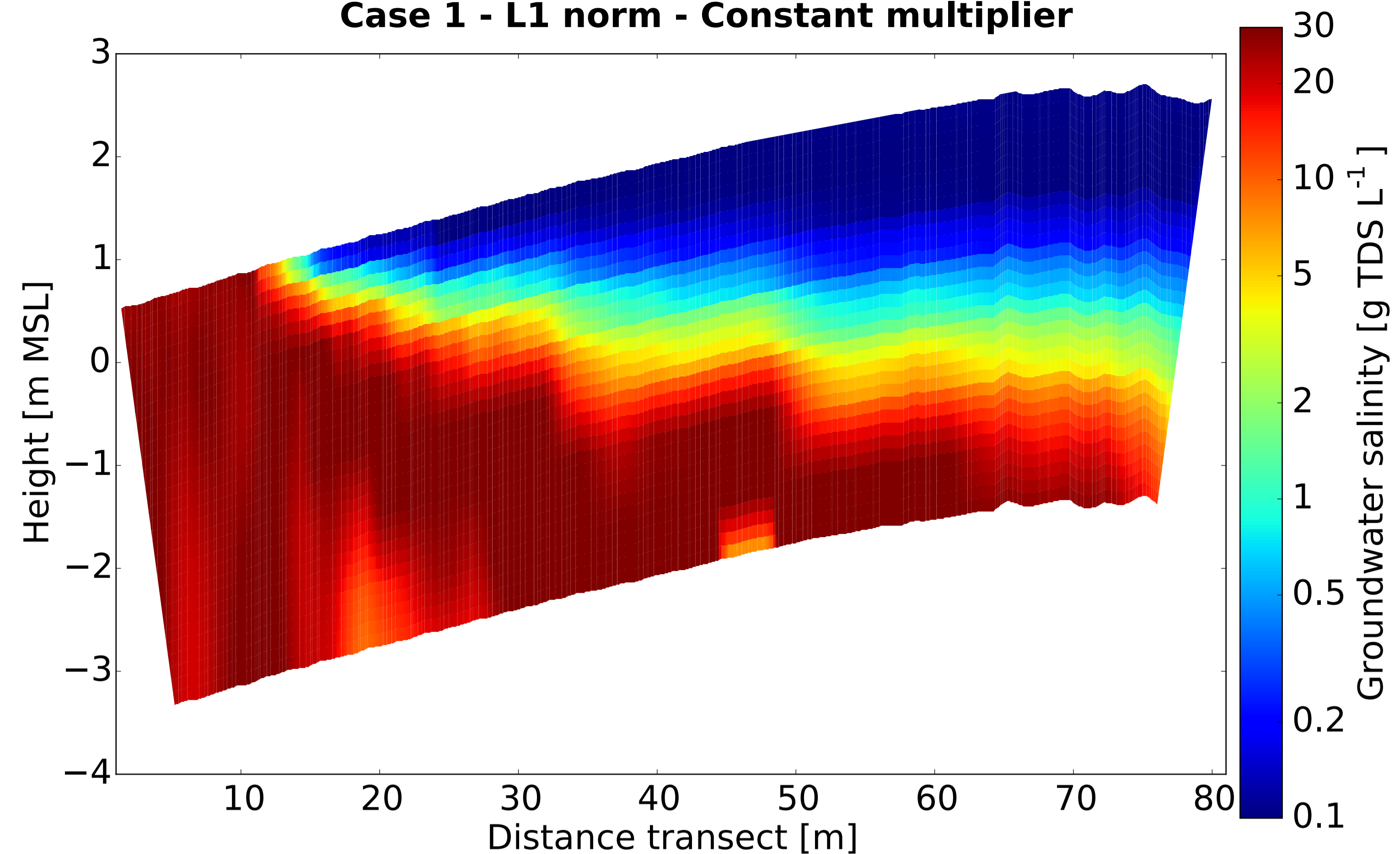




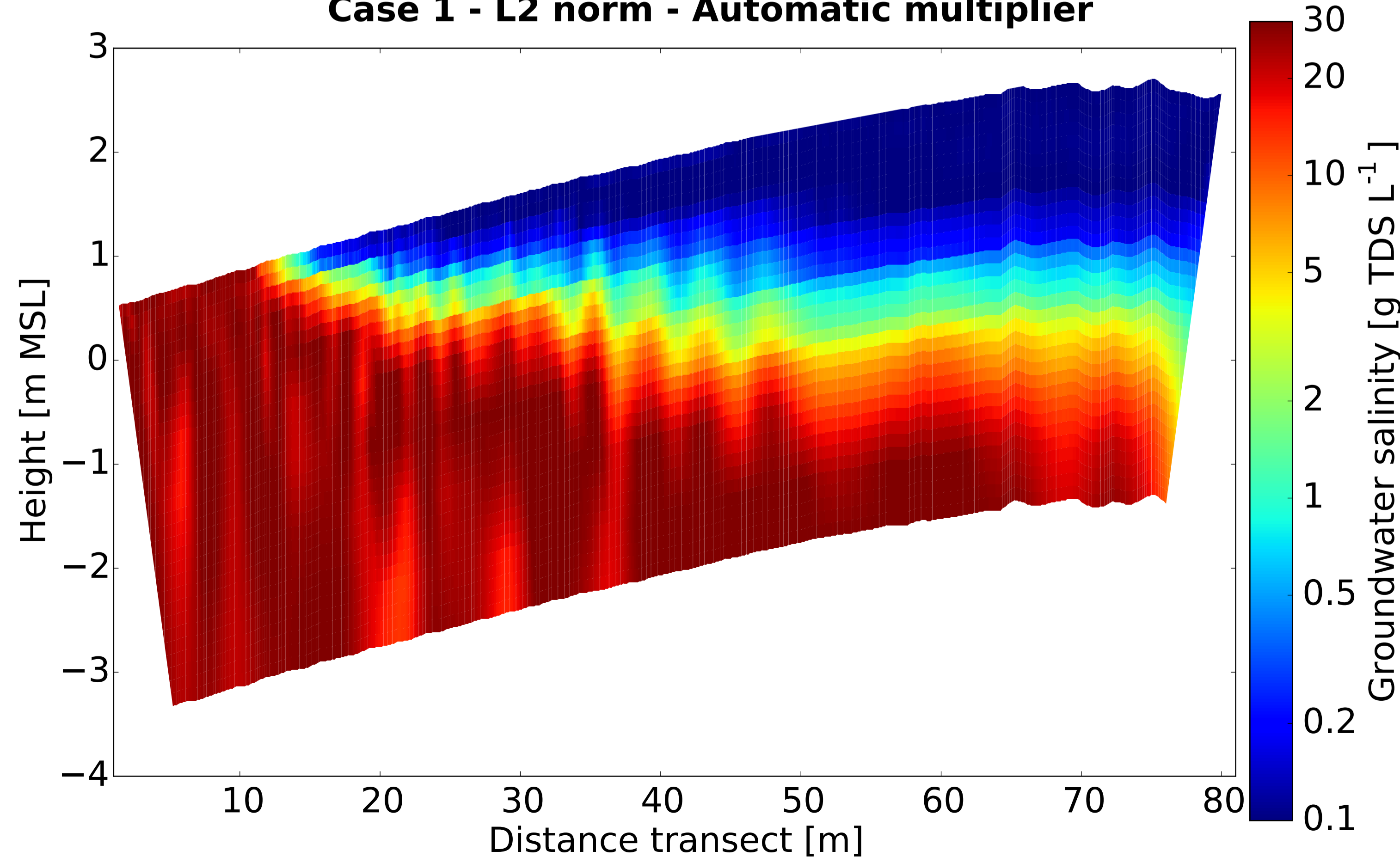
Case 1 - L1 norm - Automatic multiplier



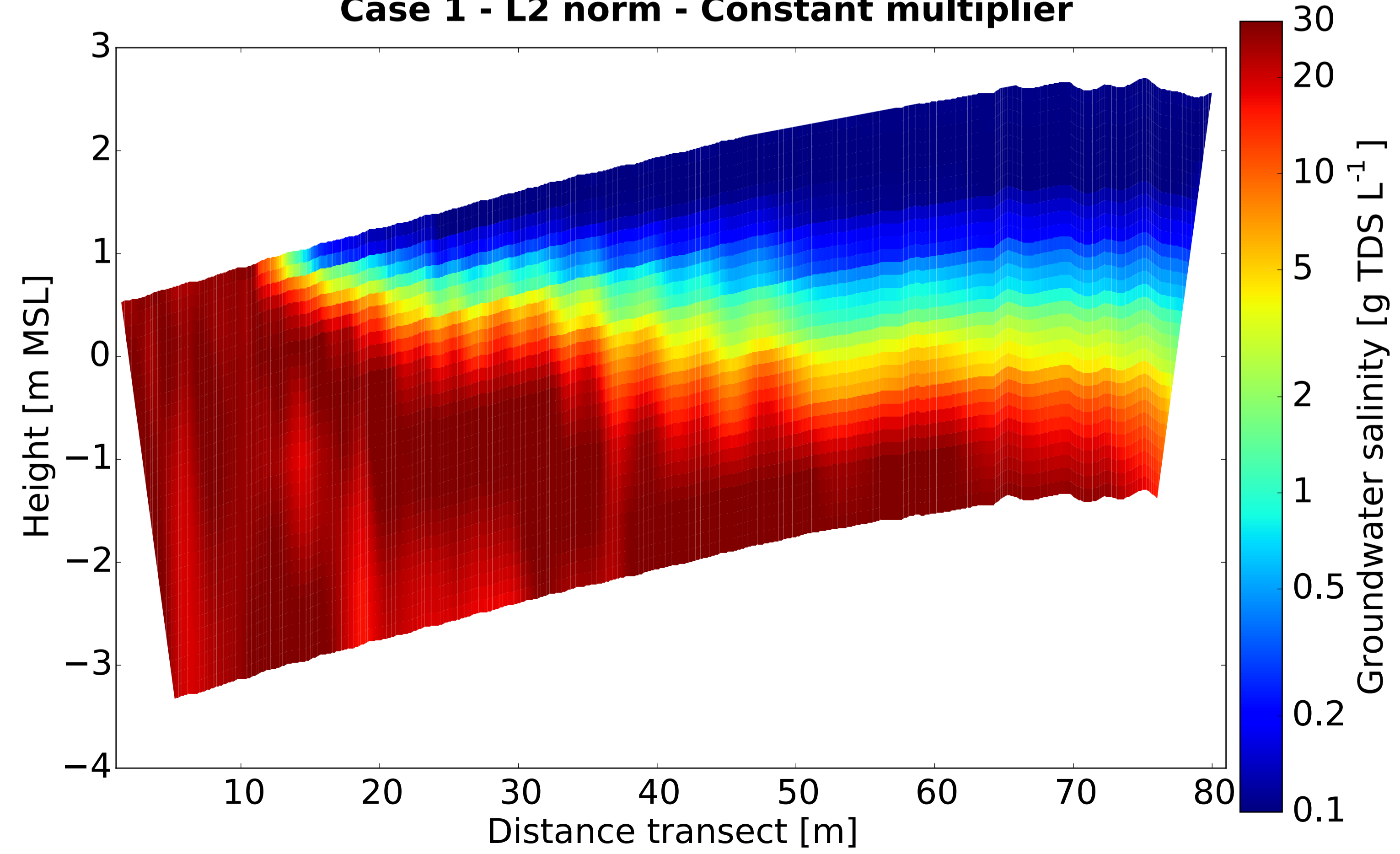
Case 1 - L1 norm - Constant multiplier



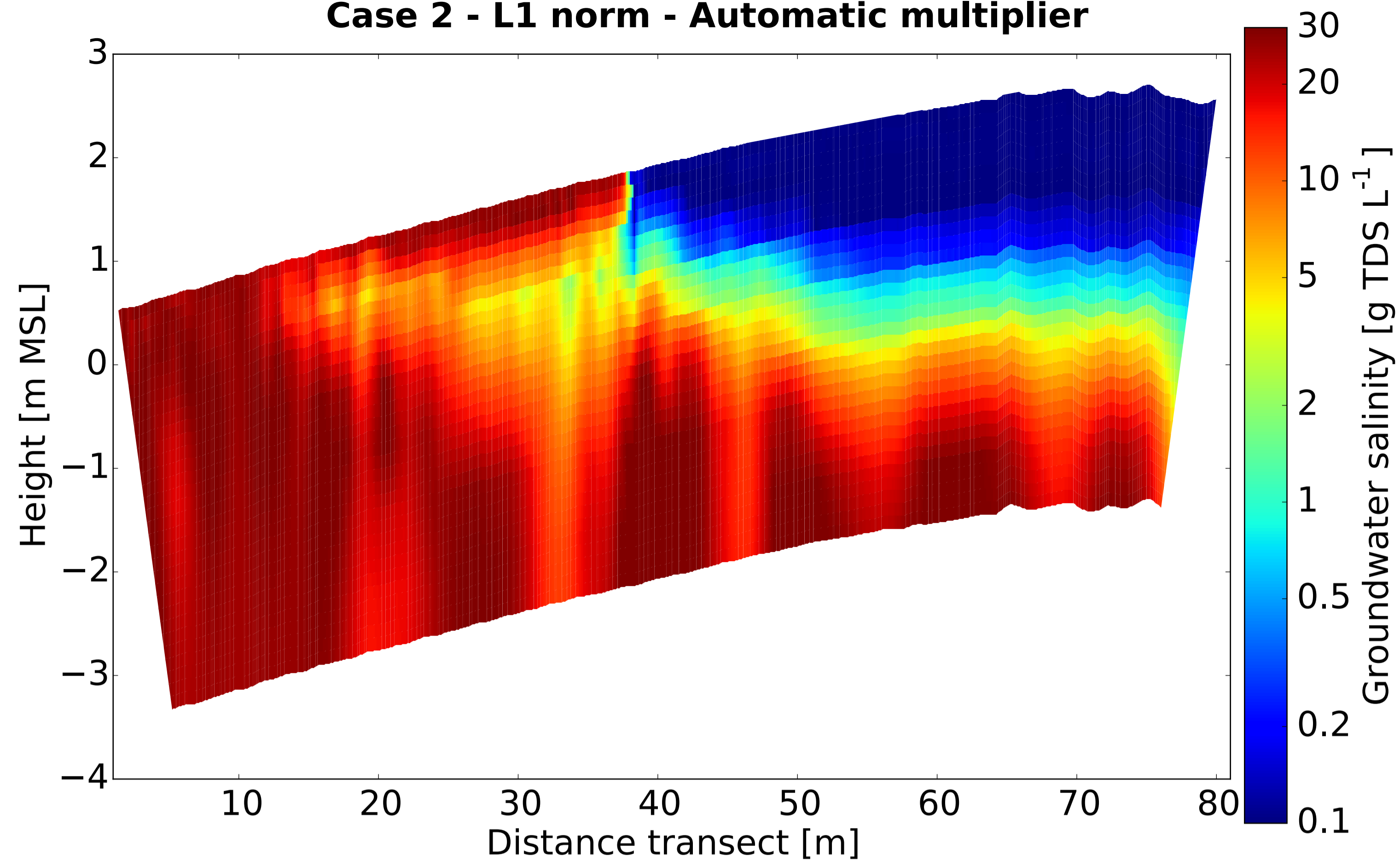
Case 1 - L2 norm - Automatic multiplier



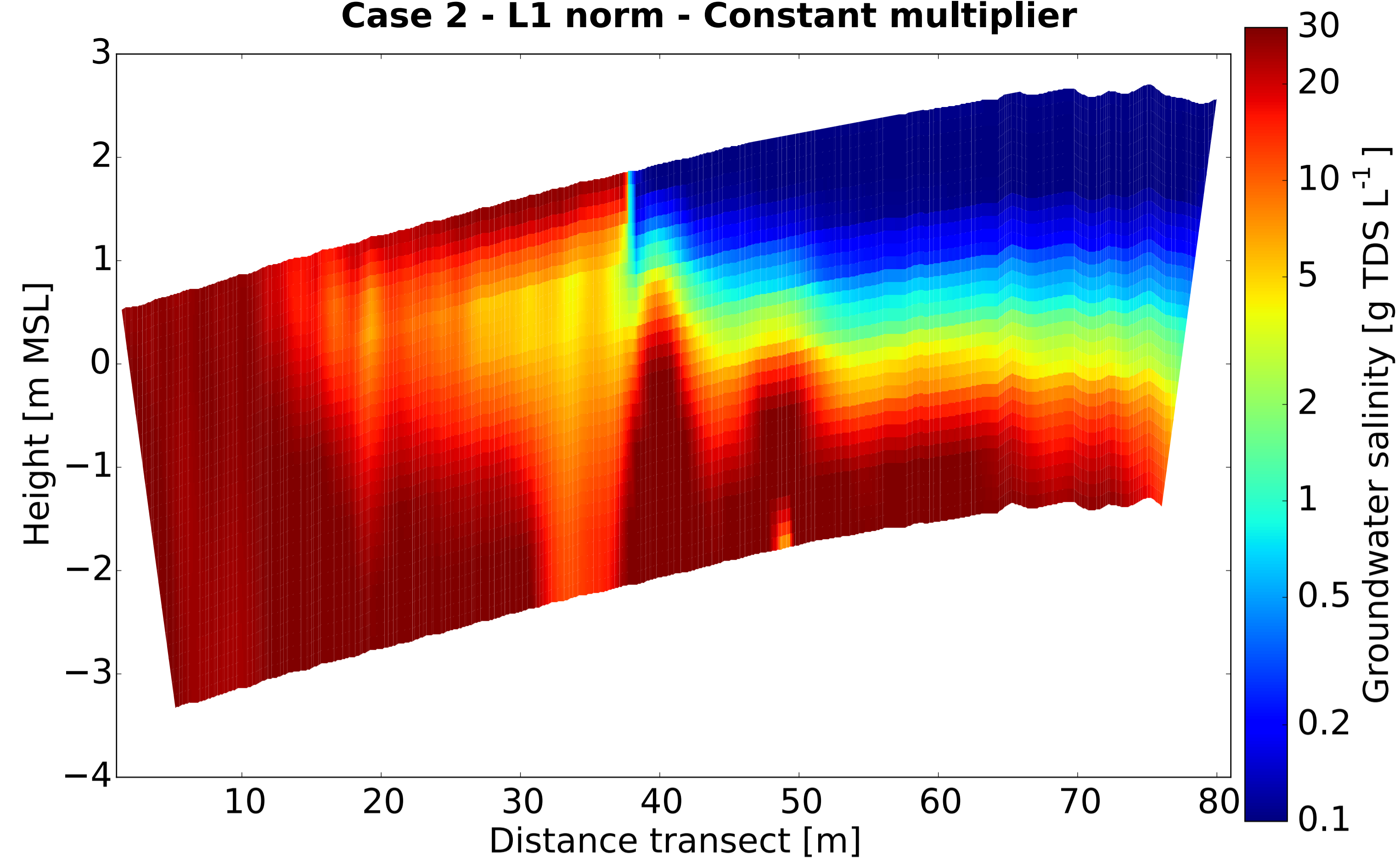
Case 1 - L2 norm - Constant multiplier



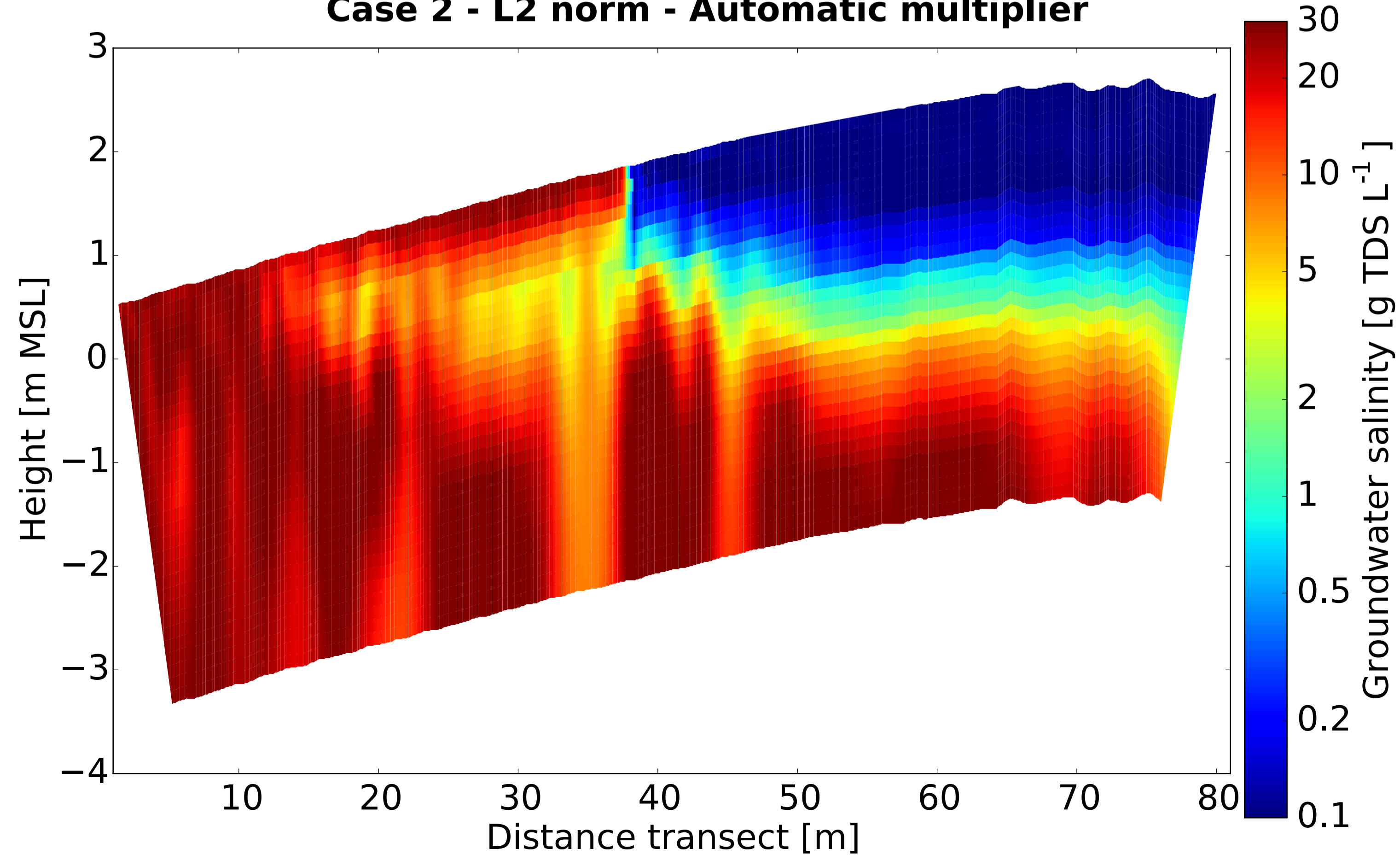
Case 2 - L1 norm - Automatic multiplier



Case 2 - L1 norm - Constant multiplier



Case 2 - L2 norm - Automatic multiplier



Case 2 - L2 norm - Constant multiplier

